








Rapidly rotating stars and their transiting planets: KELT-17b, KELT-19Ab, and KELT-21b in the *CHEOPS* and *TESS* era

Z. Garai ^{1,2,3,4}★ T. Pribulla ³, J. Kovács ^{1,2,4}, Gy. M. Szabó ^{1,2,4}, A. Claret ^{5,6}, R. Komžík ³ and E. Kundra ³

¹MTA-ELTE Exoplanet Research Group, 9700 Szombathely, Szent Imre h. u. 112, Hungary

²ELTE Gothard Astrophysical Observatory, 9700 Szombathely, Szent Imre h. u. 112, Hungary

³Astronomical Institute, Slovak Academy of Sciences, 05960 Tatranská Lomnica, Slovakia

⁴MTA-ELTE Lendület Milky Way Research Group, 9700 Szombathely, Szent Imre h. u. 112, Hungary

⁵Instituto de Astrofísica de Andalucía, CSIC, Apartado 3004, E-18080 Granada, Spain

⁶Dept. Física Teórica y del Cosmos, Universidad de Granada, Campus de Fuentenueva s/n, E-10871 Granada, Spain

Accepted 2022 April 15. Received 2022 March 29; in original form 2021 December 17

ABSTRACT

Rapidly rotating early-type main-sequence stars with transiting planets are interesting in many aspects. Unfortunately, several astrophysical effects in such systems are not well understood yet. Therefore, we performed a photometric mini-survey of three rapidly rotating stars with transiting planets, namely KELT-17b, KELT-19Ab, and KELT-21b, using the *Characterising Exoplanets Satellite (CHEOPS)*, complemented with *Transiting Exoplanet Survey Satellite (TESS)* data, and spectroscopic data. We aimed at investigating the spin-orbit misalignment and its photometrical signs, therefore the high-quality light curves of the selected objects were tested for transit asymmetry, transit duration variations, and orbital precession. In addition, we performed transit time variation analyses, obtained new stellar parameters, and refined the system parameters. For KELT-17b and KELT-19Ab, we obtained significantly smaller planet radius as found before. The gravity-darkening effect is very small compared to the precision of *CHEOPS* data. We can report only on a tentative detection of the stellar inclination of KELT-21, which is about 60 deg. In KELT-17b and KELT-19Ab, we were able to exclude long-term transit duration variations causing orbital precession. The shorter transit duration of KELT-19Ab compared to the discovery paper is probably a consequence of a smaller planet radius. KELT-21b is promising from this viewpoint, but further precise observations are needed. We did not find any convincing evidence for additional objects in the systems.

Key words: methods: observational – techniques: photometric – techniques: spectroscopic – planets and satellites: individual: KELT-17b, KELT-19Ab, KELT-21b.

1 INTRODUCTION

Early-type main-sequence stars are rapidly rotating stars. Late-type stars (F5 and later) have deep convective envelopes and efficient magnetic dynamos, maintaining magnetic fields that transfer angular momentum to the stellar wind, thus slowing down the star’s surface through magnetic braking. This is the so-called Kraft break (Kraft 1967). The rapid rotation at early-type stars leads to an oblate shape of the star and induces an equator-to-pole gradient in the effective temperature, called gravity darkening (Von Zeipel 1924a, b). The so-called von Zeipel theorem predicts that the flux emitted from the surface is proportional to the local effective gravity, thus the effect induces cooler temperatures at a rapidly rotating star’s equator and hotter temperatures at the poles. However, the von Zeipel theorem is not strictly valid, hence it needs further investigation. Claret (1998) found important deviations from von Zeipel theorem in stars with envelopes in convective equilibrium. Moreover, Claret (2012) found significant deviations from von Zeipel theorem at the upper layers of a distorted star in radiative equilibrium. If an exoplanet transits a

rapidly rotating star, distorted transit light curves are expected, as it was predicted by Barnes (2009). If such asymmetries are measured, this can be used to determine the sky-projected angle λ between the stellar rotational axis and the planet orbit normal, i.e. we can detect the spin-orbit misalignment. In addition, the stellar inclination I_* , which we define as the angle between the line of sight to the observer and the north pole of the star, can be derived and thus the true misalignment is possible to obtain. Another way to investigate the sky-projected spin-orbit misalignment is to measure the Rossiter–McLaughlin effect via radial velocities (McLaughlin 1924; Rossiter 1924). We can note, however, that radial velocity measurements in the case of early-type stars are difficult due to the rapid rotation. In the case of rapidly rotating stars the Doppler tomography in spectral line profiles, broadening function (BF) profiles, or least-squares deconvolution profiles is applicable. With this technique the shadow of the transiting planet can also be detected, independently from the photometry (Donati et al. 1997). Both techniques – photometric and spectroscopic – can be used to put constraints on the theories of planet formation and migration.

Szabó et al. (2011) found an asymmetry in the rapidly rotating Kepler-13A transit light curve, consistent with the prediction of Barnes (2009). Kepler-13A is the first known system, exhibiting

* E-mail: zgarai@ta3.sk, zgarai@gothard.hu

a light-curve distortion due to spin-orbit misalignment and gravity darkening of a rapidly rotating star. Barnes, Linscott & Shporer (2011) used this asymmetry to measure the sky-projected spin-orbit misalignment angle λ . They determined $\lambda = 23 \pm 4$ deg, and $I_* = 138 \pm 4$ deg,¹ which gives the real misalignment of 56 ± 4 deg. This represents the first spin-orbit measurement obtained based on precise *Kepler* photometry (Borucki et al. 1996, 2004), although later Johnson et al. (2014) obtained $\lambda = 58 \pm 2$ deg via Doppler tomography, which is a significantly different value for the sky-projected spin-orbit misalignment angle. Moreover, the stellar rotation of Kepler-13A is in exact 5:3 resonance with the orbital period of the substellar companion, and the long-term transit duration variation (TDV) with a rate of $(1.14 \pm 0.30) \times 10^{-6}$ d cycle⁻¹ is due to the precession of its orbital plane (Szabó et al. 2012). This long-term trend in the transit duration was confirmed using combined *Kepler* and *Transiting Exoplanet Survey Satellite* (*TESS*) data (Ricker 2014) by Szabó et al. (2020). We can say that the system Kepler-13A is a unique laboratory of many astrophysical effects.

Recently, for example, the asymmetric transit of the exoplanet KELT-9b was obtained and modelled using *TESS* data (Ahlers et al. 2020). KELT-9b is an ultra-hot Jupiter transiting a rapidly rotating early A-type star in a polar orbit (Gaudi et al. 2017). This is the main reason, why KELT-9b is an interesting planet. The true spin-orbit misalignment angle was determined as 87 ± 11 deg by Ahlers et al. (2020). Another rapidly rotating A-type star with a transiting planet, i.e. WASP-189b, was observed also very recently using the *Characterising Exoplanets Satellite* (*CHEOPS*) space observatory (Benz et al. 2021). From the asymmetric transit photometry of WASP-189b Lendl et al. (2020) deduced the sky-projected spin-orbit misalignment angle of $\lambda = 86.4 \pm 4.4$ deg and the true misalignment of 85.4 ± 4.3 deg, in a good agreement with the previous measurement from spectroscopic observation (Anderson et al. 2018). This result indicates that WASP-189b is in a polar orbit, similarly as KELT-9b. Since rapidly rotating early-type main-sequence stars with transiting planets can be similar to the ‘prototype’ Kepler-13A system, in 2019 we proposed a mini-survey of such exoplanet hosts using the *CHEOPS* space telescope, to constrain their planetary and stellar parameters, and to characterize the star-planet interactions in these cases. For this mini-survey we selected KELT-17, KELT-19A, and KELT-21 planetary systems. Fundamental facts about the exoplanet host stars are summarized in Table 1.

KELT-17b is a $1.3 M_{\text{Jup}}$ and a $1.5 R_{\text{Jup}}$ hot Jupiter, transiting the $V = 9.23$ mag main-sequence A-star KELT-17 in a 3.08-d misaligned orbit at $\lambda = 244.0$ deg, discovered by Zhou et al. (2016). The host star BD + 14° 1881 ($M_* = 1.6 M_{\odot}$, $T_{\text{eff}} = 7454$ K, $v \sin I_* = 44.2$ km s⁻¹) is one of the most massive, hottest, and most rapidly rotating planet host stars. KELT-19Ab transits the $V = 9.86$ mag main-sequence A-star KELT-19A in a 4.61-d retrograde orbit ($\lambda = 180.3$ deg). The host star BD + 07° 1721 is the first chemically peculiar Am-star, which hosts a hot-Jupiter-type planet with a mass of $M_p < 4.07 M_{\text{Jup}}$ and a radius of about $1.9 R_{\text{Jup}}$. Moreover, adaptive optics observations revealed a cooler stellar companion, KELT-19B, which is a G9V or K1V star. The stars have measured magnitude differences of $\Delta J = 2.50 \pm 0.06$ mag and $\Delta K_s = 2.045 \pm 0.03$ mag (Sivervd et al. 2018). The projected separation is 0.64 arcsec, so this system is a close analogue of the Kepler-13 system. KELT-21b is a $3.9 M_{\text{Jup}}$ and a $1.5 R_{\text{Jup}}$ hot Jupiter, transiting the $V = 10.5$ mag main-sequence A-star KELT-21 in a 3.6-d orbit, which is misaligned only slightly

Table 1. An overview of fundamental facts about the exoplanet host stars. Notes: H2000 = Høg et al. (2000), G2018 = Gaia Collaboration (2018).

| Parameter [unit] | Value | Source |
|--------------------------|------------------|--------|
| KELT-17 (BD + 14° 1881) | | |
| RA [h:m:s] (J2000.0) | 08:22:28.2 | G2018 |
| Dec. [deg:m:s] (J2000.0) | +13:44:07.1 | G2018 |
| V [mag] | 9.23 ± 0.02 | H2000 |
| G [mag] | 9.2089 ± 0.0003 | G2018 |
| KELT-19A (BD + 07° 1721) | | |
| RA [h:m:s] (J2000.0) | 07:26:02.2 | G2018 |
| Dec. [deg:m:s] (J2000.0) | +07:36:56.8 | G2018 |
| V [mag] | 9.86 ± 0.04 | H2000 |
| G [mag] | 9.8633 ± 0.0016 | G2018 |
| KELT-21 (HD 332124) | | |
| RA [h:m:s] (J2000.0) | 20:19:12.0 | G2018 |
| Dec. [deg:m:s] (J2000.0) | +32:34:51.7 | G2018 |
| V [mag] | 10.48 ± 0.04 | H2000 |
| G [mag] | 10.5415 ± 0.0003 | G2018 |

($\lambda = 354.4$ deg). The host star HD 332124 has the highest projected rotational velocity among the exoplanet hosts ($v \sin I_* = 146$ km s⁻¹), and it also appears to be somewhat metal poor (Johnson et al. 2018).

In this paper, we aimed at refining the system parameters based on the obtained *CHEOPS* photometry data, supplemented with several spectroscopic observations. Furthermore, based on the precise *CHEOPS* transit light curves of the systems we aimed at searching for similar asymmetries, as it was detected in the Kepler-13A system and whether asymmetries are consistent with the prediction, coming from the previous spectroscopic results. Since the photometric follow-up observations of these systems using the *CHEOPS* telescope can also reveal TDVs, and hence the orbital precession, our further scientific goal is to search for such indicators. Finally, transit time variations (TTVs) may also be detected, testing for additional planets in the systems, therefore we also included the search for such variations in our scientific aims. The paper is organized as follows. In Section 2, a brief description of instrumentation and data reduction is given. We summarize the spectral analysis and the derived stellar parameters in Section 3. The fundamental analysis of the *CHEOPS* transits and the obtained system parameters are described and discussed in Section 4. In Section 5, we analyse the *CHEOPS* light curves from the viewpoint of spin-orbit misalignment. Search for long-term TDVs and TTVs is detailed in Section 6. We summarize our findings in Section 7.

2 OBSERVATIONS AND DATA REDUCTION

2.1 Transit photometry

The transits of KELT-17b, KELT-19Ab, and KELT-21b were observed photometrically using the *CHEOPS* space observatory (Benz et al. 2021). This is the first European space mission dedicated primarily to the study of known exoplanets. It consists of a 32 cm mirror diameter telescope² based on a Ritchey–Chrétien design. The photometric detector is a single CCD camera covering the wavelength range from 330 to 1100 nm with a field of view of 0.32 deg². The payload design and operation have been optimized to achieve ultra-high photometric stability, achieving a photometric precision of 20 ppm on observations of a G5-type star in 6 h, and 85 ppm

¹This value reflects our definition of I_* , but Barnes et al. (2011) originally presented this as follows: the north pole of the star is tilted away from the observer by 48 ± 4 deg.

²The primary mirror is partly blocked by the secondary mirror spider legs and has a central cut-out to allow the beam to pass through on to the CCD. This means that the effective mirror diameter of *CHEOPS* is 30 cm.

Table 2. Log of *CHEOPS* photometric observations of KELT-17b, KELT-19Ab, and KELT-21b transits (sorted by the targets and *CHEOPS* visits). The table shows the time interval of individual observations, the applied exposure time, the number of obtained frames, the point-to-point root mean square (*RMS*) of the DRP-processed ‘OPTIMAL’ light curves (see Section 2.1), and the file key, which supports the fast identification of the observations in the *CHEOPS* archive.

| Visit no. | Start date [UTC] | End date [UTC] | Exposure time [s] | Number of frames | <i>RMS</i> [ppm] | File key |
|-----------|------------------|------------------|-------------------|------------------|------------------|----------------------|
| KELT-17b | | | | | | |
| 1 | 2020-12-10 16:32 | 2020-12-11 01:16 | 55.1 | 330 | 420 | CH_PR210006_TG000101 |
| 2 | 2020-12-16 20:55 | 2020-12-17 04:23 | 55.1 | 300 | 420 | CH_PR210006_TG000102 |
| 3 | 2020-12-19 22:06 | 2020-12-20 06:12 | 55.1 | 292 | 380 | CH_PR210006_TG000103 |
| 4 | 2021-02-16 10:33 | 2021-02-16 18:50 | 55.1 | 339 | 280 | CH_PR210006_TG000104 |
| KELT-19Ab | | | | | | |
| 1 | 2020-11-27 12:31 | 2020-11-27 23:55 | 60.0 | 394 | 370 | CH_PR210006_TG000201 |
| 2 | 2020-12-29 19:08 | 2020-12-30 07:06 | 60.0 | 460 | 520 | CH_PR210006_TG000202 |
| 3 | 2021-01-26 11:21 | 2021-01-26 23:11 | 60.0 | 452 | 420 | CH_PR210006_TG000203 |
| 4 | 2021-01-31 01:59 | 2021-01-31 13:33 | 60.0 | 461 | 440 | CH_PR210006_TG000204 |
| KELT-21b | | | | | | |
| 1 | 2020-07-02 23:15 | 2020-07-03 08:32 | 60.0 | 333 | 720 | CH_PR210006_TG000301 |
| 2 | 2020-07-21 01:04 | 2020-07-21 10:11 | 60.0 | 370 | 780 | CH_PR210006_TG000302 |
| 3 | 2020-07-24 16:15 | 2020-07-25 01:34 | 60.0 | 379 | 720 | CH_PR210006_TG000303 |
| 4 | 2020-08-26 03:24 | 2020-08-26 13:04 | 60.0 | 390 | 920 | CH_PR210006_TG000304 |

observations of a K5-type star in 3 h. 20 per cent of the science time on *CHEOPS* is available to the astronomical community through a Guest Observers Programme that is open to the science community as a whole. *CHEOPS* observations used in this work were obtained within the first cycle of the Guest Observers Programme, proposal ID 006, entitled ‘Rapidly rotating stars and their transiting planets: a unique laboratory of many astrophysical effects’³ (PI: Z. Garai).

Based on the literature transit duration values (Zhou et al. 2016; Johnson et al. 2018; Siverd et al. 2018), at least 0.1-long phase interval is needed at every transit event (phases 0.95–1.05 around the mid-transit time) to properly cover the transit and the neighbour out-of-transit phases with observations. Therefore, we proposed five orbits⁴ per visit⁵ and four visits in the case of KELT-17b, seven orbits per visit and four visits in the case of KELT-19Ab, and six orbits per visit and four visits in the case of KELT-21b, 72 orbits in total, including interruptions.⁶ Due to the interruptions several phase gaps occurred during a single visit. The predicted observing efficiencies⁷ were 59 per cent, 58 per cent, and 63 per cent in the cases of KELT-17b, KELT-19Ab, and KELT-21b, respectively. Further details about the *CHEOPS* observations can be found in Table 2.

From the *CHEOPS* detector, which has 1024×1024 pixels, a 200×200 pixels subarray is extracted around the target point spread function, which is used to compute the photometry (see Fig. 1). The *CHEOPS* Data Reduction Pipeline – DRP (Hoyer et al. 2020) provides aperture photometry of these subarray frames. It performs several image corrections, including bias-, dark-, and flat-corrections,

³See the list of approved programs at <https://www.cosmos.esa.int/web/cheops-s-guest-observers-programme/ao-1-programmes>.

⁴*CHEOPS* revolves around the Earth in Sun-synchronous, low-Earth orbit (700 km altitude). The spacecraft completes one orbit around the Earth in 99 min.

⁵A visit is a sequence of successive *CHEOPS* orbits devoted to observing a given target.

⁶Interruptions happen when the target is hidden by the Earth during an Earth occultation, or barely visible due to stray light from the illuminated Earth limb or particle hits during passages through the South Atlantic anomaly.

⁷The observing efficiency is the ratio between the amount of science observing time available during a visit (excluding the interruptions) and the total amount of time in a visit (including the interruptions).

contamination estimation, and background-star correction. The DRP produces four different light curve types for each visit: ‘DEFAULT’ – estimated using the default aperture radius of 25 pixels, ‘OPTIMAL’ – the aperture radius is automatically set based on the signal-to-noise ratio, ‘RINF’ – using the aperture radius of 0.9×25 pixels, and ‘RSUP’ – using the aperture radius of 1.2×25 pixels. According to the relatively long exposure times (55.1 and 60.0 s), the data were transferred to the Earth without stacking the individual images together, which means that the so-called imaggettes with a smaller radius of 30 pixels are not available in these cases.

The DRP-processed *CHEOPS* light curves were downloaded from the *CHEOPS* Archive Browser.⁸ We first ran several modelling tests using the RMF code, described in Section 5, in order to select the best light-curve type offered by the archive. Since there is no significant difference among the light-curve types from the viewpoint of precision, we decided to use the ‘OPTIMAL’ light curves during our analysis procedure.

2.2 Target spectroscopy

Besides the transit photometry, spectra of the exoplanet hosts were also recorded several times to characterize these stars. The spectroscopic observations were obtained at the Skalnaté Pleso Observatory (Slovakia), using the 1.3 m f/8.36 Astelco Alt-azimuthal Nasmyth-Cassegrain reflecting telescope, equipped with a fibre-fed echelle spectrograph of MUSICOS design (Baudrand & Bohm 1992). Its fibre injection and guiding unit (FIGU) is mounted in the Nasmyth focus of the telescope. The FIGU is connected to the calibration unit (ThAr hollow cathode lamp, tungsten lamp, blue LED) in the control room and to the echelle spectrograph itself in the room below the dome, where the temperature is stable. The spectra were recorded by an Andor iKon-936 DZH 2048×2048 pixels CCD camera. The spectral range of the instrument is 4250–7375 Å in 56 echelle orders. The maximum resolution of the spectrograph reaches $R \approx 38\,000$ around 6000 Å. The exposure time was 900 s in all cases. Three raw spectra were obtained consecutively during an observing night.

⁸See <https://cheops-archive.astro.unige.ch/archive-browser/>.

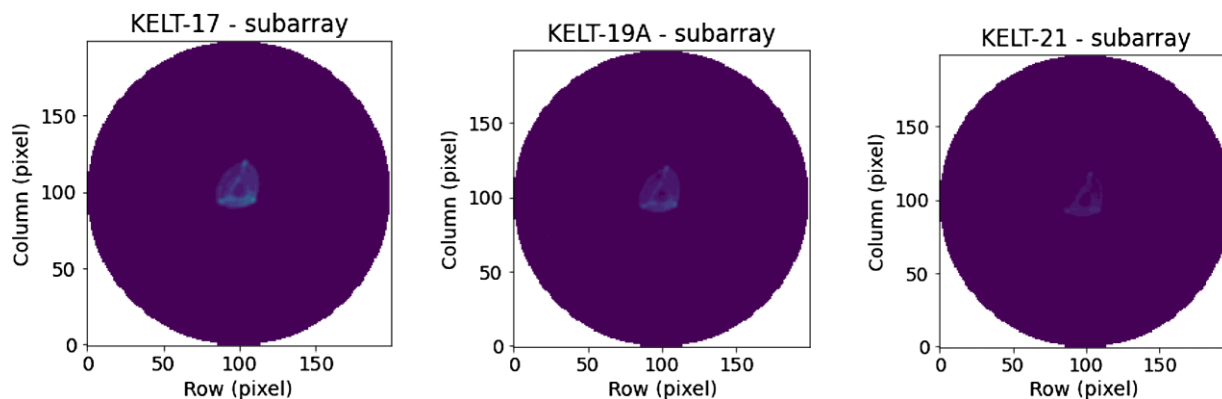


Figure 1. The 200×200 pixels subarrays of the target stars. The background stars were removed from the field of view. We can see the typical *CHEOPS* shape of stars. The point spread function is deliberately defocused to spread the flux over a number of pixels. In this way, the telescope is less sensitive to inter-pixel variation and differences in flat fielding, just like other instruments. The distortion, i.e. the triangular shape, is due to the way in which the primary mirror is supported. For more details see Benz et al. (2021).

Table 3. Log of spectroscopic observations of KELT-17, KELT-19A, and KELT-21 (sorted by the targets). The table shows the time interval of observations and the signal-to-noise ratio (S/N) of the combined spectra at 5500 \AA . The S/N was calculated as $S/N = \sqrt{(S/N)_1^2 + (S/N)_2^2 + (S/N)_3^2}$, where $(S/N)_n$ is the signal-to-noise ratio of individual spectra.

| Start date [UTC] | End date [UTC] | S/N |
|---------------------|---------------------|-------|
| KELT-17 | | |
| 2020-02-20 21:40:23 | 2020-02-20 22:28:27 | 46.5 |
| 2020-03-05 19:20:11 | 2020-03-05 20:08:10 | 30.3 |
| 2020-03-17 20:39:25 | 2020-03-17 21:27:24 | 42.8 |
| 2020-11-25 03:19:07 | 2020-11-25 04:07:07 | 38.0 |
| 2021-01-11 02:41:40 | 2021-01-11 03:29:40 | 38.0 |
| 2021-01-31 21:49:15 | 2021-01-31 22:37:16 | 48.7 |
| 2021-02-20 22:11:30 | 2021-02-20 22:59:29 | 44.6 |
| 2021-02-22 21:09:22 | 2021-02-22 21:57:22 | 40.5 |
| KELT-19A | | |
| 2020-02-08 21:17:29 | 2020-02-08 22:05:29 | 38.5 |
| 2020-02-20 19:44:45 | 2020-02-20 20:33:33 | 30.9 |
| 2020-03-17 19:06:11 | 2020-03-17 19:54:11 | 31.3 |
| 2020-12-02 01:23:02 | 2020-12-02 02:11:02 | 38.3 |
| 2020-12-13 00:35:12 | 2020-12-13 01:23:12 | 40.2 |
| 2020-12-19 23:42:37 | 2020-12-20 00:30:37 | 44.5 |
| 2021-01-10 23:54:41 | 2021-01-11 00:42:40 | 30.0 |
| 2021-02-21 18:44:05 | 2021-02-21 19:32:06 | 37.5 |
| 2021-02-22 19:33:07 | 2021-02-22 20:21:08 | 29.9 |
| KELT-21 | | |
| 2020-07-05 22:30:27 | 2020-07-05 23:18:28 | 25.8 |
| 2020-07-30 22:40:10 | 2020-07-30 23:28:05 | 17.3 |
| 2020-08-01 22:32:39 | 2020-08-01 23:15:38 | 23.2 |
| 2020-08-12 22:56:31 | 2020-08-12 23:44:32 | 27.7 |
| 2020-09-14 20:33:48 | 2020-09-14 21:21:48 | 24.3 |
| 2020-10-28 16:31:23 | 2020-10-28 17:19:23 | 22.5 |
| 2020-11-09 17:46:08 | 2020-11-09 18:36:14 | 29.1 |
| 2020-11-10 17:04:23 | 2020-11-10 17:52:24 | 27.6 |

More details about the spectroscopic observations can be found in the observations log (see Table 3).

The raw spectra were reduced using *IRAF* package tasks, *LINUX* shell scripts, and *FORTTRAN* programs similarly, as it was described in Pribulla et al. (2015) and in Garai et al. (2017). In the first step, master dark frames were produced. In the second step, the photometric calibration of the frames was done using dark and flat-field frames. Bad pixels were cleaned using a bad pixel mask, and cosmic hits were removed using the program of Pych (2004). Order positions

were defined by fitting Chebyshev polynomials to tungsten lamp and blue LED spectrum. In the following step, scattered light was modelled and subtracted. Aperture spectra were then extracted for both object and ThAr frames, and then the resulting 2D spectra were dispersion-solved. Two-dimensional spectra were finally combined to 1D spectra rebinned to $4250\text{--}7375 \text{ \AA}$ wavelength range with a 0.05 \AA step, i.e. about two to four times the spectral resolution.

The obtained 1D spectra were combined to increase the signal-to-noise ratio using *iSpec*⁹ (Blanco-Cuaresma et al. 2014; Blanco-Cuaresma 2019). As first, three consecutive spectra of the same night were combined with the assumption that there is no substantial difference (Doppler shift) between them. For the following steps, we used these averaged (median) spectra. We shifted all of the spectra (KELT-17–8 spectra, KELT-19A–9 spectra, KELT-21–8 spectra) into the rest frame combined the barycentric correction and the intrinsic radial velocity correction into one step applying the *ISPEC* cross-correlation routine. We cross-correlated the spectra with a template from the Munari et al. (2005) synthetic spectrum library. According to the literature values for the stellar parameters, i.e. the effective temperature, the surface gravity, and metallicity (Zhou et al. 2016; Johnson et al. 2018; Siverd et al. 2018), all three host stars are very similar, therefore we selected the template file from the spectrum library, which corresponds to $T_{\text{eff}} = 7500 \text{ K}$, $\log g = 4.0 \text{ cgs}$, and $[M/H] = -0.5 \text{ dex}$. After shifting the spectra into the rest frame we averaged them via median into a final spectrum per object with setting the resolution to $R = 20000$ (average resolution of the spectrograph), and setting the sampling to 0.05 \AA . We then corrected for the depression between 4800 and 5540 \AA (KELT-17 and KELT-19A), and slightly shifted the overall continuum level upward with a value of about 0.02 to set it to be 1.0 as much as possible. In this way, we obtained the final averaged spectra for the host stars, which we further analysed to obtain basic stellar parameters (see Section 3).

3 STELLAR PARAMETERS FROM SPECTRA

3.1 Data analysis

We tried to fit the final averaged spectra with several spectral synthesis softwares, but only the *FASMA*¹⁰ code (Andreasen et al. 2017; Tsantaki et al. 2018) led to reasonable results. This could

⁹See <https://www.blancocuaresma.com/s/iSpec>.

¹⁰See <http://www.iastro.pt/fasma/>.

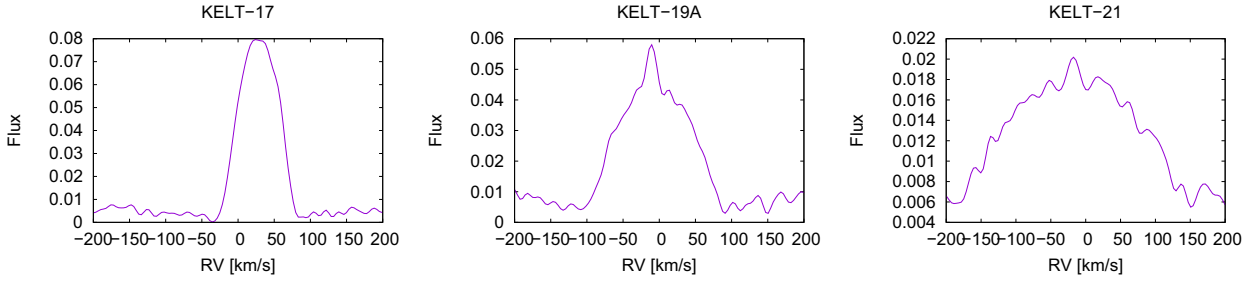


Figure 2. Selected BFs of the host stars, smoothed differently, according to the rotational velocities. The radial velocities are barycentric. The secondary component KELT-19B is well visible as a narrow peak on top of the broad profile of the primary component KELT-19A.

be due to the relatively high temperature of the host stars. The spectral synthesis softwares, e.g. *SPECTRUM* (Gray & Corbally 1994), *ISPEC* (Blanco-Cuaresma et al. 2014; Blanco-Cuaresma 2019), or *SME* (Valenti & Piskunov 1996), work more effectively for the spectra with T_{eff} between 5000 and 6000 K. The spectroscopic analysis in the *FASMA* software is based on the spectral synthesis technique using the radiative transfer code *MOOG*.¹¹ The model atmospheres are generated by the *ATLAS9* program¹² (Mészáros et al. 2012), and all grids are based on 1D atmosphere in LTE. *FASMA* includes the parameter optimization procedure based on the Levenberg–Marquardt algorithm. Uncertainties on fitted parameters are estimated applying the covariance matrix method, see Gonzalez & Laws (2000) and Gonzalez & Vanture (1998).

The software offers the option to the user either to provide initial guesses for the parameters or set the spectral type and luminosity class of the star. We used the first option and set the starting parameters as follows. Since the host stars are very similar, we uniformly set the effective temperature ($T_{\text{eff}} = 7500$ K), the surface gravity ($\log g = 4.0$ cgs), metallicity ($[\text{Fe}/\text{H}] = 0.0$ dex), and the stellar microturbulent velocity ($v_{\text{mic}} = 1.0$ km s⁻¹). The stellar macroturbulent velocity was fixed during the analysis to the value of $v_{\text{mac}} = 0.0$ km s⁻¹, which is justified by the radiative envelopes of A-type stars and by the definition of the macroturbulent velocity in *FASMA*, which describes the motion in larger atmospheric cells (Tsantaki et al. 2018). We did not adjust the projected rotational velocity during the analysis, as well. This parameter was derived based on the BF technique (Rucinski 1992) and then we adopted and fixed. Examples of BFs are depicted in the panels of Fig. 2. For KELT-17 we obtained $v \sin I_* = 48.49 \pm 0.15$ km s⁻¹, in the case of KELT-19A we got $v \sin I_* = 86.36 \pm 0.21$ km s⁻¹, and for KELT-21 we derived $v \sin I_* = 141.9 \pm 2.4$ km s⁻¹. In the latter case we used 99 km s⁻¹ in the software, because this is the possible upper limit in *FASMA*. If $v \sin I_*$ is set to zero at the start of the fitting process, it will increase systematically at each step until it reaches the numerical limit of the program, so it would probably be closer to the true value of about 141 km s⁻¹ if the program did not have this limit. We tested the effect of this constraint on the fitted parameters during calculations, where the $v \sin I_*$ parameter was fixed to the values of 50, 60, 70, 80, 90, and 99 km s⁻¹. We found that $v \sin I_* > 60$ km s⁻¹ has negligible effect on the fitted parameters. Finally, we can note that the procedure is relatively independent from the initial conditions and the starting parameters affect only the computing time of the fitting procedure.

Table 4. An overview of the stellar parameters obtained from the spectra of KELT-17, KELT-19A, and KELT-21, compared to the previously published parameters.

| Parameter [unit] | This work | Zhou et al. (2016) |
|-------------------------------------|------------------|-----------------------|
| KELT-17 | | |
| $M_* [M_\odot]$ | – | 1.635 ± 0.066 |
| $R_* [R_\odot]$ | – | 1.645 ± 0.060 |
| $I_* [\text{deg}]$ | – | 94 ± 10 |
| $T_{\text{eff}} [\text{K}]$ | 7109 ± 252 | 7454 ± 49 |
| $\log g [\text{cgs}]$ | 4.28 ± 0.39 | 4.220 ± 0.024 |
| $\text{Fe}/\text{H} [\text{dex}]$ | -0.08 ± 0.12 | -0.018 ± 0.074 |
| $v_{\text{mic}} [\text{km s}^{-1}]$ | 3.31 ± 0.35 | – |
| $v \sin I_* [\text{km s}^{-1}]$ | 48.49 ± 0.15 | 44.2 ± 1.5 |
| Parameter [unit] | This work | Siverv et al. (2018) |
| KELT-19A | | |
| $M_* [M_\odot]$ | – | 1.62 ± 0.25 |
| $R_* [R_\odot]$ | – | 1.830 ± 0.099 |
| $T_{\text{eff}} [\text{K}]$ | 6643 ± 391 | 7500 ± 110 |
| $\log g [\text{cgs}]$ | 3.56 ± 0.63 | 4.127 ± 0.029 |
| $\text{Fe}/\text{H} [\text{dex}]$ | -0.38 ± 0.21 | -0.12 ± 0.51 |
| $v_{\text{mic}} [\text{km s}^{-1}]$ | 2.62 ± 0.42 | – |
| $v \sin I_* [\text{km s}^{-1}]$ | 86.36 ± 0.21 | 84.8 ± 2.0 |
| Parameter [unit] | This work | Johnson et al. (2018) |
| KELT-21 | | |
| $M_* [M_\odot]$ | – | 1.458 ± 0.029 |
| $R_* [R_\odot]$ | – | 1.638 ± 0.034 |
| $T_{\text{eff}} [\text{K}]$ | 8210 ± 771 | 7598 ± 84 |
| $\log g [\text{cgs}]$ | 4.53 ± 1.12 | 4.173 ± 0.015 |
| $\text{Fe}/\text{H} [\text{dex}]$ | -0.19 ± 0.36 | -0.405 ± 0.033 |
| $v_{\text{mic}} [\text{km s}^{-1}]$ | 0.68 ± 1.08 | – |
| $v \sin I_* [\text{km s}^{-1}]$ | 141.9 ± 2.4 | 146.03 ± 0.48 |

3.2 Results of target spectroscopy

The obtained parameters are summarized and compared to the previously published parameters in Table 4. We briefly discuss these parameters in the following subsections. The observed and averaged stellar spectra, overlapped with the synthetic spectra are depicted in the Figs 3 and 4.

3.2.1 KELT-17

KELT-17 has a mass of $1.635 \pm 0.066 M_\odot$ and a radius of $1.645 \pm 0.060 R_\odot$ (Zhou et al. 2016). Based on an independent differential rotation analysis, presented by Zhou et al. (2016), there is some information about the stellar inclination of KELT-17. They found $I_* = 94 \pm 10$ deg, which means that the star is seen

¹¹ See <https://www.as.utexas.edu/~chris/moog.html>.

¹² See <http://research.iac.es/proyecto/ATLAS-APOGEE/>.

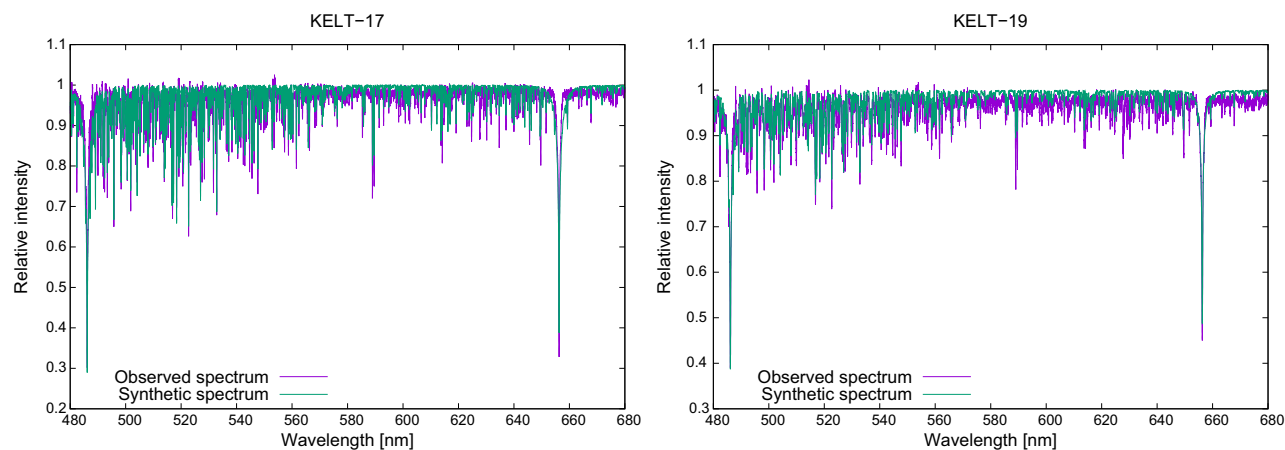


Figure 3. The final averaged spectrum of the host stars KELT-17 (left-hand panel) and KELT-19A (right-hand panel), overplotted with the synthetic spectrum.

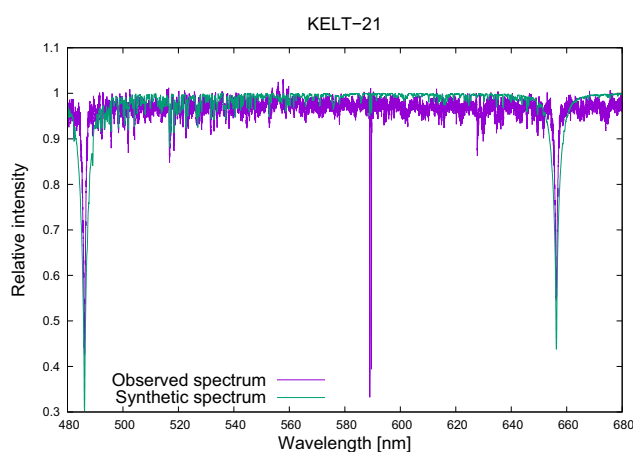


Figure 4. As in Fig. 3, but for KELT-21.

nearly equator-on. Using the `FASMA` code we obtained the stellar parameters of $T_{\text{eff}} = 7109 \pm 252$ K, $\log g = 4.28 \pm 0.39$ cgs, $[\text{Fe}/\text{H}] = -0.08 \pm 0.12$ dex, and $v_{\text{mic}} = 3.31 \pm 0.35$ km s⁻¹, which are in a 3σ agreement with the previously derived stellar parameters, obtained by Zhou et al. (2016).

3.2.2 KELT-19A

As noted in Section 1, KELT-19 is a visual double star. The host star is the primary component KELT-19A, which has peculiar abundance pattern that is indicative of it belonging to the class of metallic-line mean sequence Am stars (Siverd et al. 2018). It has a mass of $1.62 \pm 0.25 M_{\odot}$ and a radius of $1.830 \pm 0.099 R_{\odot}$ as derived by the discoverers. Since the star rotates faster than KELT-17, the parameters are determined less precisely than in the previous case. Moreover, spectrum of KELT-19A includes light contamination from the companion star KELT-19B, which is a cooler G-, or K-type mean sequence star. This means a possible systematic bias, even if the secondary component contributes with a very low signal to the composite spectrum. The light contribution of the companion depends on the seeing conditions. Its parameters are quite uncertain, thus difficult to disentangle the spectrum. These conditions allowed us to obtain the following stellar parameters with `FASMA`: $T_{\text{eff}} = 6643 \pm 391$ K, $\log g = 3.56 \pm 0.63$ cgs, $[\text{Fe}/\text{H}] = -0.38 \pm 0.21$

dex, and $v_{\text{mic}} = 2.62 \pm 0.42$ km s⁻¹. The parameters are in a 3σ agreement to those of derived by Siverd et al. (2018).

3.2.3 KELT-21

KELT-21 was also analysed using the `FASMA` software. This is the most rapid rotator in our sample, therefore several stellar parameters are determined poorly, or with a more than 3σ difference in comparison with the previously derived parameters, obtained by Johnson et al. (2018). KELT-21 is metal poor, which is unusual for relatively young hot stars (Johnson et al. 2018). Adaptive optics imaging reveal two likely companions of KELT-21 in the projected distance of about 1.2 arcsec, but the possible KELT-21B and KELT-21C companions are much fainter than KELT-21. The contrast is about 7.3 mag, hence they should have a negligible effect on the spectrum of the host star. The main problem at this star, which affects the stellar synthesis, is the rapid rotation with $v \sin I_* = 141.9 \pm 2.4$ km s⁻¹. Other derived stellar parameters are $T_{\text{eff}} = 8210 \pm 771$ K, $\log g = 4.53 \pm 1.12$ cgs, $[\text{Fe}/\text{H}] = -0.19 \pm 0.36$ dex, and $v_{\text{mic}} = 0.68 \pm 1.08$ km s⁻¹. The mass of the star is $1.458 \pm 0.029 M_{\odot}$ and its radius is $1.638 \pm 0.034 R_{\odot}$ (Johnson et al. 2018).

4 SYSTEM PARAMETERS FROM CHEOPS TRANSITS

4.1 Individual transit analysis

To derive the system parameters, we used the dedicated `CHEOPS` transit analysis software called `pycheops`¹³ (Maxted et al. 2022). This `PYTHON`¹⁴ package includes downloading, visualizing, and decorrelating `CHEOPS` data, fitting transits, and eclipses of exoplanets, and calculating light curve noise. We first cleaned the light curves from outlier data points using the `pycheops` built-in function `clip_outliers`, which removes outliers from a data set by calculating the mean absolute deviation (*MAD*) from the light curve following median smoothing, and rejects data greater than the smoothed data set plus the *MAD* multiplied by a clipping factor. The clipping factor equal to five was reasonable in our cases, which we checked visually. The next step was the roll angle effect subtraction.

¹³See <https://github.com/pmaxted/pycheops>.

¹⁴See <https://www.python.org/>.

In order to keep the cold plate radiators facing away from the Earth, the spacecraft rolls during its orbit. This causes that the field of view rotates around the pointing direction. The target star remains stationary within typically a pixel, but the rotation of the field of view produces a variation of its flux from the nearby sources in phase with the roll angle of the spacecraft (Bonfanti et al. 2021). At exoplanet transits this is usually a small fraction of the total flux, in a form of short-term, non-astrophysical flux trends – waves or bumps. This rolling effect is not corrected by the DRP, but it is possible to perform this correction using the `PYCHEOPS` function called `DECORR`. By this ‘derolling’ procedure the *RMS* of the light-curve residuals decreased by about 30–50 ppm. Subsequently, the residuals were visually checked against the roll angle to ensure that the removal of rolling systematics has been done properly. Using this function it is possible to model first-, second-, or third-order trends in the flux over time, x or y centroid, roll angle, background, or contamination. After the decorrelation process the data are ready for model fitting.

We first fitted the transit light curves individually. The `PYCHEOPS` package uses the `qpower2` transit model with the power-2 limb-darkening law (Maxted 2018; Maxted & Gill 2019). Transit models are constructed using the following transit parameters: the orbital period P_{orb} , the mid-transit time T_c , the transit depth D , which is defined as $D = (R_p/R_s)^2$, where R_p/R_s is the planet-to-star radius ratio, the transit width W (in phase units), the impact parameter b (in units of stellar radius), which is defined as $b = a \cos i / R_s$, where a is the semimajor axis of the planet’s orbit and i is the orbit inclination angle with respect to the plane of the sky, the flux scaling factor c , the limb-darkening coefficients h_1 and h_2 , and the orbital eccentricity and longitude of periastron components $f_c = e \cos \omega / \sqrt{e}$ and $f_s = e \sin \omega / \sqrt{e}$, where e is the eccentricity and ω is the longitude of periastron. Several decorrelation parameters are also used. During the individual transit analysis we fixed the orbital period P_{orb} using the already published literature values (Zhou et al. 2016; Johnson et al. 2018; Siverd et al. 2018). We also did not adjust the limb-darkening coefficient h_2 , which was interpolated from the stellar parameters (T_{eff} , $\log g$, and Fe/H), tabulated in the `SWEET-Cat` data base (Santos et al. 2013) using the `ATLAS` model, see e.g. Claret (2018). We note that prior this treatment we ran several test modellings with h_2 allowed to float, however, we always got unphysical fitted coefficient far from the interpolated value and the corresponding fit was inappropriate. Very probably this is due to the high T_{eff} of the planet hosts. Finally, we decided to keep fixed this coefficient, which reflects the average temperatures of the stars. The average temperatures are closer to the lowest temperature, because the polar star regions, where is the highest effective temperature, have the smallest area. We assumed circular orbit for KELT-17b, KELT-19Ab, and KELT-21b, thus the f_c and f_s parameters were set to zero. Other parameters were freely adjusted.

The final parameters were derived using a Markov chain Monte Carlo (MCMC) methodology. The software `PYCHEOPS` does this by utilizing the affine invariant sampler `PYTHON` package `EMCEE`¹⁵ (Foreman-Mackey et al. 2013) to sample the posterior probability distribution of fitting the constructed transit model to the data. The best-fitting values from the `qpower2` analysis are used as priors for the `EMCEE` sampler function. The sampler has built-in functionality to fit and remove correlated stellar noise using a Gaussian process regression method from the `CELERITE2`¹⁶ package (Kallinger et al. 2014; Foreman-Mackey et al. 2017; Barros et al. 2020). The regres-

sion is done by using a `SHOTerm` plus `JitterTerm` kernel, with a fixed quality factor $Q = 1/\sqrt{2}$, implemented in the `CELERITE2` package. It uses $\log \sigma$ (free), $\log Q$ (fixed), $\log \omega_0$ (free), and $\log S_0$ (free) hyperparameters with bounds on the values of these parameters to be inputted by the user. We first fixed the transit shape, i.e. the parameters D , W , and b , and the mid-transit time T_c from the initial `qpower2` fit and set free the three hyperparameters for a preliminary MCMC analysis. The posteriors of the hyperparameters obtained from this analysis were used to define the priors for the next MCMC analysis as twice the uncertainty computed from the posterior distribution. Finally, we ran the MCMC analysis again with free transit model parameters and free hyperparameters.

4.2 Joint transit analysis

To combine the best-fitting results obtained from the individual `CHEOPS` light curves and to get final parameters of the exoplanet systems, we performed a joint analysis of the data set per object using the `PYCHEOPS` package. Because the observations were obtained at multiple epochs, in this case we fitted not only the transit shape, i.e. the parameters D , W , and b , and the mid-transit time T_c , but also the orbital period P_{orb} of the planet. As during the individual analysis, we fitted only the limb-darkening coefficient h_1 and fixed h_2 as interpolated from the stellar parameters, and we also fixed the f_c and f_s parameters to zero. We also used the decorrelation parameters of each single visit, and the Gaussian process regression method from the `CELERITE2` package, with the common hyperparameters of $\log \omega_0$ and $\log S_0$. The priors on the hyperparameters were determined as the average (with error propagation) of the single-visit hyperparameters. We note that in the joint transit analysis mode, the roll angle model is not part of the detrending model as in the individual transit analysis mode. The detrending parameters of the roll angle (and its harmonics) are treated as nuisance parameter (Luger, Foreman-Mackey & Hogg 2017) and they are marginalized away as a `CELERITE2` `CosineTerm` kernel added to the covariance matrix. This method implicitly assumes that the roll angle is a linear function of time for each visit. The results obtained from this joint transit analysis are presented in Section 4.3.

As the next step we took the best-fitting parameters of T_c and P_{orb} from the joint analysis and used them as fixed parameters for calculating TTVs based on the joint model. In this case the `PYCHEOPS` software fits the transit shape as previously during the joint transit analysis, but in addition, it also fits the deviation $\Delta T_{0,n}$ for the n -th visit from the calculated individual mid-transit time. The observed mid-transit time $T_{0,n}$ is defined based on the linear ephemeris as:

$$T_{0,n} = T_c + P_{\text{orb}} \times E + \Delta T_{0,n}, \quad (1)$$

where E is the epoch of observation, i.e. the number of the orbital cycle. The fitted $\Delta T_{0,n}$ value corresponds to the observed-minus-calculated (O-C) value of mid-transit time, which is a very effective tool to reveal TTVs of planets through the O-C diagram. The `CHEOPS` space telescope can be used for this purpose as it was recently discussed by Borsato et al. (2021). The transit timing analysis of the data is detailed in Section 6.2.

4.3 Overview and discussion of the refined system parameters

We summarize the fitted and derived parameters of the planetary systems in Table 5. We also present the previously published parameters for easy comparison. The phase-folded transit light curves of the exoplanets KELT-17b, KELT-19Ab, and KELT-21b, overplotted with the best-fitting `PYCHEOPS` models are presented in Figs 5 and 6.

¹⁵See <https://emcee.readthedocs.io/en/stable/>.

¹⁶See <https://celerite.readthedocs.io/en/stable/>.

Table 5. An overview of the PYCHEOPS best-fitting and derived parameters of the exoplanets KELT-17b, KELT-19Ab, and KELT-21b obtained from the *CHEOPS* photometry, compared to the previously published parameters. Notes: ¹The closest mid-transit time to the mid-point of the *CHEOPS* data set; ²Adopted from literature; ³Derived based on $K = 131 \pm 29 \text{ m s}^{-1}$ (Zhou et al. 2016). ⁴Derived based on $K < 352 \text{ m s}^{-1}$ (Sivverd et al. 2018). ⁵Derived based on $K < 400 \text{ m s}^{-1}$ (Johnson et al. 2018). The best-fitting P_{orb} values are preliminary, see Section 6.2 for improved values.

| Parameter [unit] | Prior | This work | Zhou et al. (2016) |
|----------------------------------|-----------------------------|-------------------------------|------------------------------|
| KELT-17b | | | |
| T_c [BJD _{TDB}] | $N(2459215.9375, 0.0004)^1$ | $2459215.937950 \pm 0.000086$ | $2457226.14219 \pm 0.00033$ |
| P_{orb} [d] | $N(3.0801718, 0.0000053)^2$ | 3.0801724 ± 0.0000047 | 3.0801718 ± 0.0000053 |
| D | $N(0.0085, 0.0001)$ | 0.008482 ± 0.000049 | 0.00907 ± 0.00017 |
| W (in phase units) | $N(0.047, 0.001)$ | 0.04691 ± 0.00013 | 0.04701 ± 0.00045 |
| b (in units of stellar radius) | $N(0.60, 0.03)$ | 0.587 ± 0.011 | 0.570 ± 0.035 |
| h_1 | $N(0.79, 0.10)$ | 0.7657 ± 0.0094 | – |
| h_2 (fixed) | 0.557 | 0.557 | – |
| R_p/R_s | – | 0.0921 ± 0.0011 | 0.09526 ± 0.00088 |
| a/R_s | – | 6.246 ± 0.077 | 6.38 ± 0.18 |
| R_p [R _{Jup}] | – | 1.507 ± 0.055 | 1.525 ± 0.065 |
| M_p [M _{Jup}] | – | 1.31 ± 0.29^3 | 1.31 ± 0.29 |
| $\log g_p$ | – | 3.154 ± 0.099 | 3.14 ± 0.11 |
| ρ_p [g cm ⁻³] | – | 0.47 ± 0.11 | 0.46 ± 0.12 |
| Parameter [unit] | Prior | This work | Sivverd et al. (2018) |
| KELT-19Ab | | | |
| T_c [BJD _{TDB}] | $N(2459218.1780, 0.0005)^1$ | $2459218.17799 \pm 0.00013$ | $2457281.24953 \pm 0.00036$ |
| P_{orb} [d] | $N(4.6117093, 0.0000088)^2$ | 4.6117105 ± 0.0000077 | 4.6117093 ± 0.0000088 |
| D | $N(0.0100, 0.0002)$ | 0.009702 ± 0.000061 | 0.01148 ± 0.00020 |
| W (in phase units) | $N(0.038, 0.001)$ | 0.03791 ± 0.00010 | 0.03970 ± 0.00032 |
| b (in units of stellar radius) | $N(0.55, 0.03)$ | 0.499 ± 0.018 | 0.601 ± 0.030 |
| h_1 | $N(0.79, 0.10)$ | 0.8064 ± 0.0087 | – |
| h_2 (fixed) | 0.542 | 0.542 | – |
| R_p/R_s | – | 0.0985 ± 0.0010 | 0.10713 ± 0.00092 |
| a/R_s | – | 8.213 ± 0.088 | 7.50 ± 0.20 |
| R_p [R _{Jup}] | – | 1.794 ± 0.097 | 1.91 ± 0.11 |
| M_p [M _{Jup}] | – | $<4.10^4$ | <4.07 |
| $\log g_p$ | – | <3.61 | <3.44 |
| ρ_p [g cm ⁻³] | – | <1.30 | <0.744 |
| Parameter [unit] | Prior | This work | Johnson et al. (2018) |
| KELT-21b | | | |
| T_c [BJD _{TDB}] | $N(2459055.3524, 0.0001)^1$ | $2459055.352380 \pm 0.000086$ | $2457382.640727 \pm 0.00041$ |
| P_{orb} [d] | $N(3.6127647, 0.0000033)^2$ | 3.6127640 ± 0.0000031 | 3.6127647 ± 0.0000033 |
| D | $N(0.0100, 0.0001)$ | 0.009757 ± 0.000054 | 0.00990 ± 0.00014 |
| W (in phase units) | $N(0.047, 0.001)$ | 0.04722 ± 0.00013 | 0.04734 ± 0.00025 |
| b (in units of stellar radius) | $N(0.40, 0.01)$ | 0.4044 ± 0.0095 | 0.423 ± 0.039 |
| h_1 | $N(0.80, 0.10)$ | 0.7627 ± 0.0089 | – |
| h_2 (fixed) | 0.569 | 0.569 | – |
| R_p/R_s | – | 0.0987 ± 0.0011 | 0.09952 ± 0.00073 |
| a/R_s | – | 6.885 ± 0.081 | 6.86 ± 0.13 |
| R_p [R _{Jup}] | – | 1.610 ± 0.034 | 1.586 ± 0.040 |
| M_p [M _{Jup}] | – | $<3.70^5$ | <3.91 |
| $\log g_p$ | – | <3.32 | <3.59 |
| ρ_p [g cm ⁻³] | – | <1.18 | <1.24 |

4.3.1 KELT-17b

Based on the *CHEOPS* observations, the planet KELT-17b is a close-in hot Jupiter with an orbital period of $P_{\text{orb}} = 3.0801724 \pm 0.0000047$ d. The orbital period was improved further in Section 6.2. It is a massive, inflated planet, its mass is $M_p = 1.31 \pm 0.29 M_{\text{Jup}}$ and its radius is $R_p = 1.507 \pm 0.055 R_{\text{Jup}}$, which gives the planet density of $\rho_p = 0.47 \pm 0.11 \text{ g cm}^{-3}$. This value is only about 35 per cent of the Jupiter’s density. Based on the *CHEOPS* measurements the planet body seems to be smaller in comparison with the value presented by the discoverers. The fitted transit depth is $D = 0.008482 \pm 0.000049$. Zhou et al. (2016) obtained the

transit depth of $D = 0.00907 \pm 0.00017$, which is about 3.4σ difference. The planet-to-star radius ratio parameter was derived from the transit depth, giving the value of $R_p/R_s = 0.0921 \pm 0.0011$. This is almost 3σ difference in comparison with the value of $R_p/R_s = 0.09526 \pm 0.00088$, presented by the discoverers. This is an interesting result, suggesting that the planet is not so inflated as found before. On the other hand, this also could be due either to the difference in spectral response of the applied detectors, or the reason could be a parameter degeneracy between D and b . The disadvantage of *CHEOPS* observations from this viewpoint is the lack of multicolour data. Other fitted and derived parameters are in

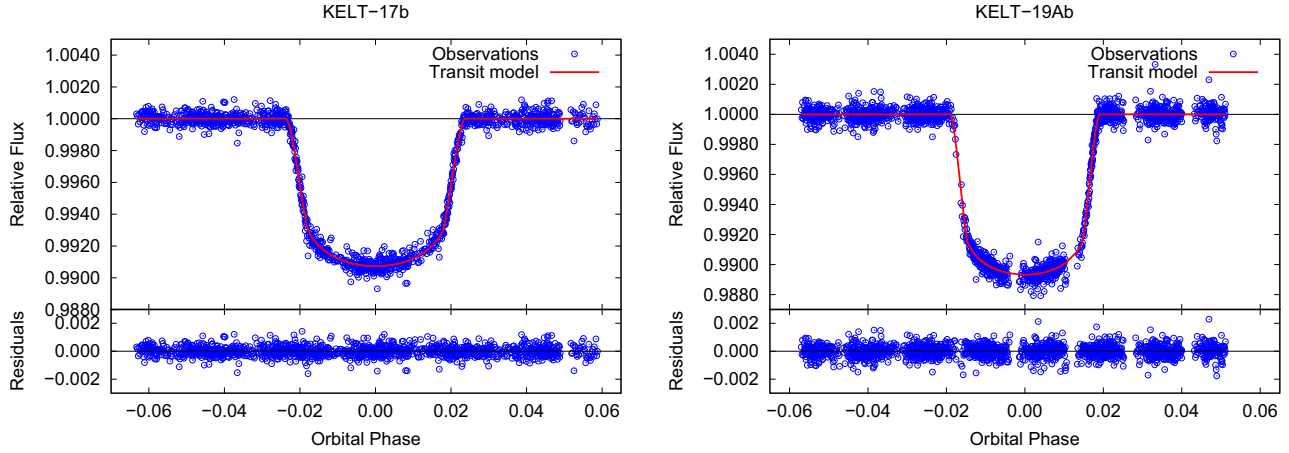


Figure 5. Phase-folded *CHEOPS* transit light curves of KELT-17b (left-hand panel) and KELT-19Ab (right-hand panel), overplotted with the best-fitting *PYCHEOPS* models. Residuals are also shown (bottom panels). During the joint modelling procedure all individual *CHEOPS* light curves were combined and fitted simultaneously.

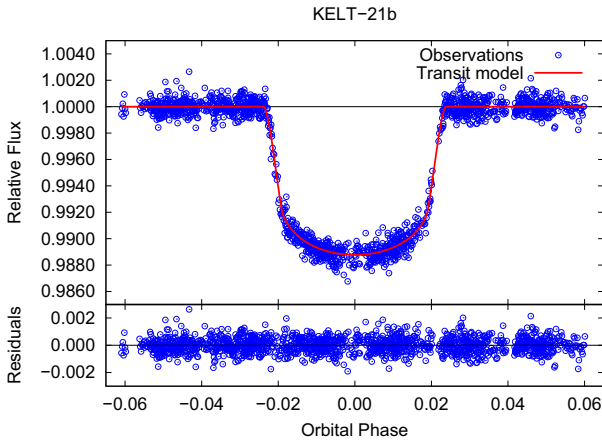


Figure 6. As in Fig. 5, but for KELT-21b.

a 3σ agreement with the discovery paper, but we improved several parameter values in comparison with Zhou et al. (2016), for example in the case of a/R_s with a factor of 2.3, or in the case of T_c with a factor of 3.8.

4.3.2 KELT-19Ab

KELT-19Ab is a close-in giant hot-Jupiter-type planet with an orbital period of $P_{\text{orb}} = 4.6117105 \pm 0.0000077$ d (see Section 6.2 for the improved value). This parameter value was derived based on the four *CHEOPS* observations and it is in a 3σ agreement with the orbital period found by the discoverers. Other fitted parameters are, however, significantly different in comparison with the parameter values presented by Siverd et al. (2018). This indicates that the parameter degeneracy between D and b as the reason for this discrepancy is less probable. The transit is shallower, we obtained a transit depth of $D = 0.009702 \pm 0.000061$, which is almost 9σ difference in comparison with the previously obtained value of $D = 0.01148 \pm 0.00020$. Consequently, the planet body is also smaller, the derived parameter R_p/R_s is 0.0985 ± 0.0010 , where is about 8.6σ difference in comparison with the value presented by the discoverers. Note that we could not refine only this parameter using *CHEOPS* observations. The obtained impact parameter is also very different,

i.e. we obtained $b = 0.499 \pm 0.018$, while Siverd et al. (2018) derived $b = 0.601 \pm 0.030$, which differs by about 3.4σ from our value. The scaled semimajor axis a/R_s also seems to be significantly larger by about 3.5σ . The telescope rotation cannot cause such a discrepancy, mainly because the rolling effect is too small, moreover, because the observed flux was decorrelated against the roll angle. The mass of the planet is not constrained well due to the scatter in the discovery radial velocity measurements, as well as the parameters derived from the planet mass are only upper limited (see Table 5). The last parameter, i.e. the transit width W (the transit duration) is discussed in Section 6.1.

Yang, Chary & Liu (2022) recently reported on results of a follow-up photometry observation of three exoplanets, including KELT-19Ab, using precise *TESS* data. Yang et al. (2022) analysed 2-min cadence data of KELT-19Ab and they corrected the contamination coming from the field stars using the *Gaia* data base (Gaia Collaboration 2018). The authors derived the following system parameters: $R_p/R_s = 0.09955 \pm 0.00074$, $i = 88.9 \pm 0.7$ deg, and $a/R_s = 9.10 \pm 0.19$. We can see that the planet-to-star radius ratio value derived from the *TESS* data is comparable with the R_p/R_s value obtained based on the *CHEOPS* measurements (the difference is about 1σ). On the other hand, the orbit inclination angle¹⁷ i and the scaled semimajor axis value a/R_s is significantly different from the *CHEOPS*-based values.

Furthermore, we reanalysed the mentioned *TESS* 2-min cadence data set of KELT-19Ab using the RMF code, as it is described in Section 6.1. We got $R_p/R_s = 0.09550 \pm 0.00030$, $i = 87.65 \pm 0.36$ deg, and $a/R_s = 8.70 \pm 0.17$. These results also indicate that the size of KELT-19Ab is smaller than originally derived by the discoverers and that its orbital parameters are different, too.

4.3.3 KELT-21b

KELT-21b is a hot-Jupiter-type planet with an orbital period of $P_{\text{orb}} = 3.6127640 \pm 0.0000031$ d, improved further in Section 6.2, orbiting the host KELT-21, which is the most rapidly rotating star to host a transiting planet. Based on the newly obtained spectra

¹⁷Converting the value of $b = 0.499 \pm 0.018$, obtained based on the *CHEOPS* data, to orbit inclination angle gives $i = 86.17 \pm 0.14$ deg.

Table 6. An overview of the RMF best-fitting parameters of the exoplanets KELT-17b, KELT-19Ab, and KELT-21b obtained from the *CHEOPS* photometry and using the gravity-darkening approach of Espinosa Lara & Rieutord (2011). Notes: ¹The closest mid-transit time to the mid-point of the *CHEOPS* data set. ²Based on *pycheops* results. ³Assuming circular orbit. ⁴Based on the literature values (Zhou et al. 2016; Johnson et al. 2018; Siverd et al. 2018). ⁵Minimum value, assuming $I_* = 90$ deg. ⁶Unknown parameter, assuming $I_* = 90$ deg.

| Parameter [unit] | KELT-17b | KELT-19Ab | KELT-21b |
|--|---------------------------|-------------------------|-------------------------|
| T_c [BJD _{TDB}] ¹ | 2459215.937912 ± 0.000073 | 2459218.17800 ± 0.00012 | 2459055.35251 ± 0.00016 |
| P_{orb} [d] (fixed) ² | 3.0801724 | 4.6117105 | 3.6127640 |
| i [deg] | 84.780 ± 0.071 | 88.66 ± 0.33 | 87.19 ± 0.13 |
| R_s/a | 0.15952 ± 0.00068 | 0.1100 ± 0.0014 | 0.14357 ± 0.00090 |
| R_p/R_s | 0.09186 ± 0.00016 | 0.09640 ± 0.00021 | 0.09551 ± 0.00016 |
| e (fixed) ³ | 0.0 | 0.0 | 0.0 |
| ω [deg] (fixed) ³ | 90.0 | 90.0 | 90.0 |
| λ [deg] (0 deg if aligned; fixed) ⁴ | 244.0 | 180.3 | 354.4 |
| di/dt [deg d ⁻¹] (fixed) | 0.0 | 0.0 | 0.0 |
| $\Omega/\Omega_{\text{crit}}$ (fixed) ⁵ | 0.113 | 0.230 | 0.394 |
| I_* [deg] (fixed) ⁶ | 90.0 | 90.0 | 90.0 |
| l_{norm} | 1.0000750 ± 0.0000010 | 1.0000740 ± 0.0000010 | 1.0000760 ± 0.0000010 |
| l_3 (fixed) | 0.0 | 0.0 | 0.0 |

Table 7. Log of *TESS* observations of KELT17b, KELT-19Ab, and KELT-21b used in our analysis. The table shows time interval of observations, number of observed transits, and number of data points obtained from the *TESS* data base.

| Target | Time interval of observations | Transits | Data points |
|----------|-------------------------------|----------|-------------|
| KELT-17 | 2021-10-12–2021-12-30 | 22 | 47 411 |
| KELT-19A | 2019-01-07–2019-02-02 | 4 | 16 362 |
| KELT-21 | 2021-07-23–2021-08-20 | 8 | 18 322 |

(see Section 2.2) we derived the $v \sin I_* = 141.9 \pm 2.4$ km s⁻¹, but Johnson et al. (2018) presented a more precise value of $v \sin I_* = 146.03 \pm 0.48$ km s⁻¹. The discoverers announced a pair of faint stars at a projected separation of 1.2 arcsec from the host, which could be a pair of stars bound with KELT-21 in a triple system. If confirmed in the future, the KELT-21 system would be very unique, with two M dwarfs and a fast-rotating A-type planet host.

Based on the *CHEOPS* observations we significantly improved the system parameters (except for the planet-to-star-radius ratio R_p/R_s parameter) in comparison with Johnson et al. (2018), e.g. the impact parameter b with a factor of 4.1, or the mid-transit time T_c with a factor of 4.7. Every parameter derived based on the *CHEOPS* observations is in a 3σ agreement with the corresponding parameter value presented by the discoverers. Based on the improved parameters, KELT-21b is a massive Jupiter-sized planet with $R_p = 1.610 \pm 0.034 R_{\text{Jup}}$, transiting the host in a distance of $a = 6.885 \pm 0.081 R_s$ with the impact parameter of $b = 0.4044 \pm 0.0095$, causing the transit depth of $D = 0.009757 \pm 0.000054$. Due to the large scatter in the discovery radial velocity measurements, caused by rapid rotation of KELT-21, we can estimate only the upper limit on the planet’s mass as $M_p < 3.70 M_{\text{Jup}}$. Similarly, the derived parameters of $\log g_p < 3.32$ cgs and $\rho_p < 1.18$ g cm⁻³ are also upper limited only, similarly as in the case of KELT-19Ab (see Table 5).

5 THE *CHEOPS* TRANSIT LIGHT CURVES FROM THE VIEWPOINT OF SPIN-ORBIT MISALIGNMENT

Rossiter–McLaughlin effect (McLaughlin 1924; Rossiter 1924) observations revealed several spin-orbit misaligned planets, see e.g. Narita et al. (2008), Hébrard et al. (2009), or Johnson et al. (2011). This technique can determine only the sky-projected spin-

orbit misalignment angle λ ; moreover, due to the rapid rotation of early-type stars the radial velocity measurements are challenging in these cases. Therefore, at fast rotators the transit photometry method (Barnes 2009) is used instead of radial velocities, if the data are precise enough, see e.g. Szabó et al. (2011). The advantage of this method is that it is also possible to derive the stellar inclination I_* , and thus the true misalignment (Barnes et al. 2011). Several *CHEOPS* observations were also used for this purpose, for example in Lendl et al. (2020). Since the effect of rapid rotation in transit light curves are maximized at short wavelengths (Barnes 2009), the advantage of the *CHEOPS* observatory compared, e.g. with the *TESS* telescope is the bluer spectral window of the *CHEOPS* instrument.¹⁸ We also aimed at searching for photometric indicators of spin-orbit misalignment in the precise *CHEOPS* transit light curves of KELT-17b, KELT-19Ab, and KELT-21b, therefore we tested the obtained *CHEOPS* data from the viewpoint of transit asymmetry. For this purpose we used the same DRP processed ‘OPTIMAL’ light curves as in Section 4. The data were detrended as it is described in Section 4.1, i.e. using the *pycheops* function `decorr`, where mainly the rolling effect of the telescope is removed, but in this case we did not use the Gaussian process regression method to avoid overcompensation of the light curves (Borsato et al. 2021). We wanted to preserve the possible transit asymmetry with this data treatment.

The detrended *CHEOPS* transit data were analysed using the RMF (Roche Modified) code. The software was prepared based on the *ROCHE* code, which is devoted to the modelling of multi-data set observations of close eclipsing binary stars, such as radial velocities and multicolour light curves (Pribulla 2012). The RMF code was already used with success, e.g. in Szabó et al. (2020), where the spin-orbit misaligned Kepler-13A system were reanalysed using *Kepler* and *TESS* data. The software can simultaneously model multicolour light curves, radial velocities, and BFs, or least-squares deconvolved line profiles of binary stars and transiting exoplanets. Its modification to be used with the transiting exoplanets uses the Roche surface geometry with the planet gravity neglected for the host star (rotationally deformed shape) and spherical shape for the planet. The model can handle eccentric orbits, misaligned rotational axes of the components, stellar oblateness, gravity darkening due to rapid rotation

¹⁸See <https://www.cosmos.esa.int/web/cheops/performance-bandpass>.

using the analytical approach of Espinosa Lara & Rieutord (2011),¹⁹ Doppler beaming effect, advanced limb-darkening description, and third light. The synthesis of the broadening functions assumes solid-body rotation. The synthesis of the observables is performed in the plane of the sky using pixel elements. The effectiveness of the integration is increased by the adaptive phase step being more fine during the eclipses/transits.

The software uses the following parameters: the mid-transit time T_c , the orbital period P_{orb} , the orbit inclination angle i with respect to the plane of the sky, the ratio of the host radius to the semimajor axis R_s/a , the eccentricity e , the longitude of the periastron passage ω , the sky-projected spin-orbit misalignment angle λ , the orbit inclination angle change rate di/dt , the inclination angle of the stellar rotation axis I_* , the planet-to-star radius ratio R_p/R_s , the third light l_3 , defined as $l_3/(l_1 + l_2)$, the light-curve normalization factor I_{norm} , and the ratio of the stellar angular rotation velocity to the break-up velocity $\Omega/\Omega_{\text{crit}}$, which defines the rotationally deformed stellar shape and the temperature distribution on the stellar surface, see equation (1) in Szabó et al. (2020). The stellar limb darkening is described by the four-parameter model of Claret (2018) with the critical foreshortening angle approach. The limb-darkening coefficients (a_1 , a_2 , a_3 , a_4 , and μ_{crit})²⁰ were calculated for the *CHEOPS* passband using the same spherical PHOENIX-COND models as in Claret (2018). The applied coefficients were linearly interpolated from the calculated table for the local gravity and temperature for each surface pixel, based on the already published Fe/H parameter values, listed in Table 4. This is important because the local gravity and the effective temperature vary due to the stellar rotation. The local values of temperature were calculated using the approach of Espinosa Lara & Rieutord (2011) from the local gravity. The values of the polar temperature and gravity were adjusted, so the mean value of the surface distribution was close to the already published stellar parameters of T_{eff} and $\log g$, presented in Table 4. These coefficients were fixed during the fitting procedure. We also kept fixed the orbital period based on the *PSYCHEOPS* results, and the λ values as presented in the literature (Zhou et al. 2016; Johnson et al. 2018; Siverd et al. 2018). In addition, the eccentricity e was set to zero and the longitude of the periastron passage ω was fixed at 90 deg, i.e. we assumed circular orbit of the exoplanets. We assumed no change in the orbit inclination angle with time, i.e. we set di/dt to zero. The parameter $\Omega/\Omega_{\text{crit}}$ was calculated based on the stellar mass M_* and radius R_* , presented in the literature, see Table 4, and then it was fixed during the fitting procedure. We calculated the star's polar radius based on its mean radius using the equation (16) of Zahn, Ranc & Morel (2010). Since I_* is unknown parameter, even in the case of KELT-17 is very uncertain, we assumed $I_* = 90$ deg, thus we could calculate only the minimum value of $\Omega/\Omega_{\text{crit}}$. Finally, we also fix the l_3 parameter to zero, because the third light contamination was removed by the DRP.

We present the best-fitting RMF parameters of KELT-17, KELT-19A, and KELT-21 systems in Table 6. The uncertainties in the fitted parameters were derived based on the covariance matrix method. The majority of the parameter values corresponds to the *PSYCHEOPS* parameter solutions within 3σ . The phase-folded transit light curves of the exoplanets are depicted in Figs 7 and 8. We can see that

precision of the *CHEOPS* observations is insufficient to conclude on spin-orbit misalignment of the planets. The point-to-point scatter is too big to detect the transit asymmetry in the data, which is about 50, 10, and 150 ppm for KELT-17b, KELT-19Ab, and KELT-21b, respectively. The RMF and *PSYCHEOPS* models are close to each other and both satisfy the observations (see top panels in Figs 7 and 8). We did not detect the expected wave shape in the residuals, even though we binned the data points to highlight the possible asymmetry. This no detection is due to the characteristics of the systems. We at least confirmed that the gravity-darkening effect is very low in these cases. In the case of KELT-17b (see Fig. 9 left-hand panel) the spin-orbit misalignment angle is $\lambda = 244.0$ deg, which is in favour of the gravity-darkening effect, but on the other hand, the host star rotates relatively slowly with $v \sin I_* = 48.49 \pm 0.15$ km s⁻¹. KELT-19A rotates faster with $v \sin I_* = 86.36 \pm 0.21$ km s⁻¹, but the planet KELT-19Ab is in a retrograde orbit regime (see Fig. 9 middle panel), which causes very low gravity-darkening effect. The third system in our sample, KELT-21, was the most promising due to the very fast-rotating host star with $v \sin I_* = 141.9 \pm 2.4$ km s⁻¹, however the low gravity-darkening effect is caused by the almost aligned orbit regime of KELT-21b (see Fig. 9 right-hand panel). We can conclude that more precise observations are needed to detect these fine effects in the future. Furthermore, shorter wavelengths observations than the *CHEOPS* spectral window can make the detection easier. Finally, we tested the effect of a change in the inclination angle of the stellar rotation axis I_* on the quality of the fit. We set free the I_* parameter and measured the quality of the fit when I_* is changing. The χ^2 parameter was used as a goodness-of-fit indicator. In the cases of the relatively slowly rotating systems of KELT-17 and KELT-19A it does not affect the quality of the fit, thus we could not draw any conclusions for these systems. At the very fast-rotating KELT-21 system there is an indication that the inclination angle of the stellar rotation axis is $I_* \approx 60$ deg. We registered the lowest χ^2 at this value, and the quality of the fit decreased both below and above of this inclination angle value.

6 SEARCH FOR TDVS AND TTVS IN THE SYSTEMS

TDVs are possible in planetary systems with rapidly rotating host stars. In the case of the ‘prototype’ Kepler-13A system the identified long-term TDV is caused by precession of the orbital plane of the exoplanet Kepler-13Ab. The orbital precession is induced by oblateness of the host star. Szabó et al. (2012) found that the duration of Kepler-13Ab transits is gradually increasing with a rate of $(1.14 \pm 0.30) \times 10^{-6}$ d cycle⁻¹. Moreover, the authors suggested that the reason for this variation is the expected change of the impact parameter with a rate of $db/dt = -0.016 \pm 0.004$ yr⁻¹. Later, the orbital precession was confirmed by Masuda (2015). Szabó et al. (2020) revisited the impact parameter change rate using available *Kepler* and *TESS* data, and found a value of $db/dt = -0.011$ yr⁻¹. In this part of our work, we also investigated the presence of long-term TDV in KELT-17, KELT-19A, and KELT-21 systems, searching for possible orbital precession. Based on equation (12) in Szabó et al. (2012) the orbital precession probability is higher in the case of KELT-17b, where $\lambda = 244.0$ deg, and lower in the cases of KELT-19A and KELT-21, where nearly retrograde and aligned orbit was identified, respectively (Zhou et al. 2016; Johnson et al. 2018; Siverd et al. 2018).

TTVs were identified only in the case of a few hot Jupiters. The main reason for these variations is the suspected outer companions, i.e. planets and brown dwarfs, see for example Dawson et al. (2012), Nascimbeni et al. (2013), Maciejewski et al. (2013), Knutson et al.

¹⁹This model assumes that the latitudinal variation of T_{eff} only depends on a single parameter, namely the ratio of the equatorial velocity to the Keplerian velocity (the gravity darkening exponent is removed).

²⁰Parameter $\mu = \cos \theta$, where θ is the so-called foreshortening angle, which is angle between the line of sight and a normal to the stellar surface. For $\mu < \mu_{\text{crit}}$ the stellar flux is assumed to be zero, see Claret (2018).

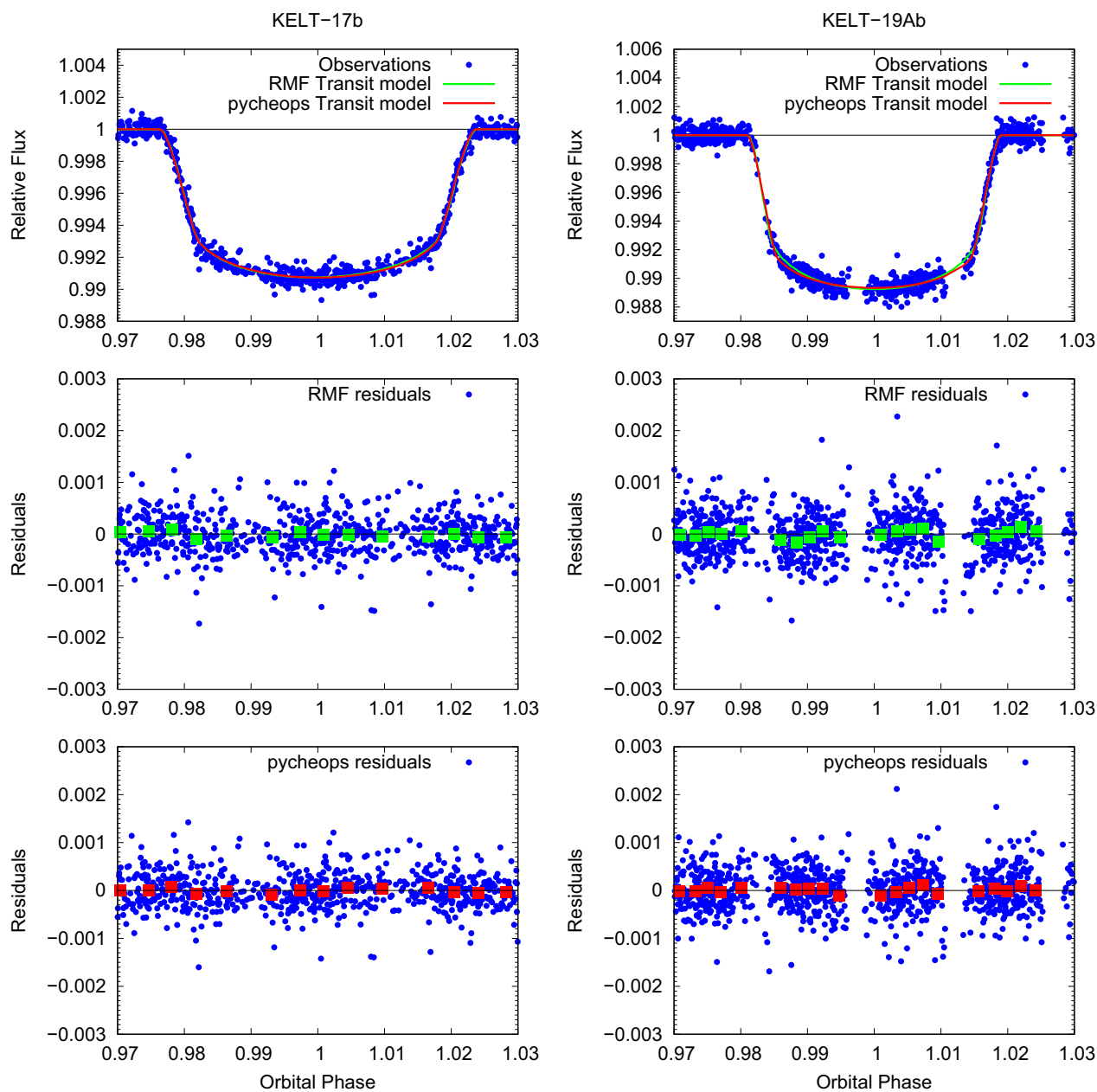


Figure 7. Phase-folded transit light curves of KELT-17b (top left-hand panel) and KELT-19Ab (top right-hand panel), overplotted with the best-fitting RMF models. The corresponding residuals are also shown (middle panels). The graphs were cropped to focus on transit events, where the asymmetry is expected. The best-fitting `PYCHEOPS` transit models (top panels) and residuals (bottom panels) are copied here for comparison purposes. The residuals were binned to highlight the possible wave shape (one bin-point represents 50 data-points).

(2014), Hartman et al. (2014), Neveu-VanMalle et al. (2016), or Gajdoš et al. (2019). Long-term TTVs were considered due to the tidal decay, for example by Hellier et al. (2009), Oberst et al. (2017), Gillon et al. (2012, 2014), or by Hebb et al. (2009); however up to now WASP-12b is the only hot Jupiter to have a decaying orbit confirmed (Turner, Ridden-Harper & Jayawardhana 2021). These examples are, however, relatively rare to the number of known hot Jupiters. Some known examples of TTVs has recently been debated, see for example Seeliger et al. (2014), Wang et al. (2018), or Ridden-Harper, Turner & Jayawardhana (2020). Szabó et al. (2020) also searched for possible TTVs in the rapidly rotating Kepler-13A system. In this particular case the absence of any TTVs is very strongly constrained by the two sources of data, i.e. *Kepler* and *TESS*. Rapid rotation as the

primary reason for the TTV signal was not confirmed within hot Jupiter planets. On the other hand, we considered as important to check the possible TTVs in the case of our sample, because precise *CHEOPS* data can uncover such a variation with higher probability.

6.1 Search for long-term TDVs – signs of orbital precession

Long-term variations in transit duration, caused by orbital precession, can be detected more easily than variations in mid-transit times, because such a long-term TDV is a linear function of time, thus longer time base-line, greater difference in transit duration (Pál & Kocsis 2008). *CHEOPS* observations of KELT-17, KELT-19A, and KELT-21 cover a time-baseline of about 2 months (see Table 2), which is

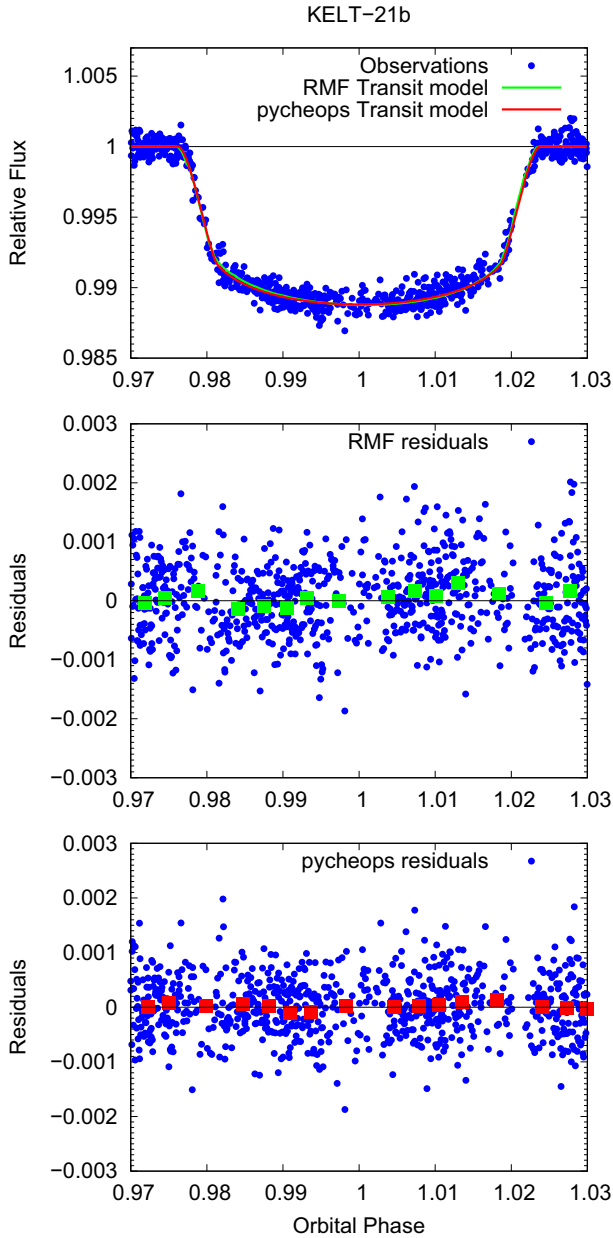


Figure 8. As in Fig. 7, but for KELT-21b.

a very short interval from this point of view. Another problem is that due to interruptions in *CHEOPS* observations (see Section 2.1) the ingress and/or the egress part of the transit light curve can be missed, thus it is not possible to search for TDVs only using the obtained *CHEOPS* data, i.e. from transit to transit. Therefore, we used the *TESS* data of these objects and the available literature data to increase the time-baseline.

KELT-17b was observed with *TESS* during three Sectors Nos. 44, 45, and 46 from 2021-10-12 to 2021-12-30. KELT-19Ab was observed in Sector No. 7 from 2019-01-07 to 2019-02-02. KELT-21b was observed in Sector No. 41 from 2021-07-23 to 2021-08-20. The data were downloaded from the Mikulski Archive for Space Telescopes²¹ in the form of Simple Aperture Photometry (SAP)

fluxes, see Table 7 for the *TESS* observational log. These data were obtained from 2-min integrations, but in comparison with Pre-search Data Conditioning Simple Aperture Photometry (PDCSAP) fluxes, long-term trends were not removed. The downloaded SAP fluxes were detrended using our pipeline, as follows. The SAP fluxes were first normalized to unity. During the next step *TESS* data were cut into segments, each covering one orbital period. Each segment of the data was fitted with a linear function. During the fitting procedure the part of the data covering the transit was excluded from the fit. Consequently, the linear trend was removed from each chunk of data (including the transit data). This detrending method can effectively remove the long-term variability (mainly variability of the host star due to spots and rotation) while it does not introduce any non-linear trend to the data, see e.g. Garai et al. (2021). Outliers were cleaned using a 3σ clipping, where σ is the standard deviation of the light curve. Since *TESS* uses as time-stamps Barycentric *TESS* Julian Date (i.e. $\text{BJD}_{\text{TDB}} - 2457000.0$), during the next step we converted all *TESS* time-stamps to BJD_{TDB} . We analysed the detrended *TESS* photometry data using the RMF code, described in Section 5. During this analysis procedure we used the same free and fixed parameters as we presented in Table 6. We applied the four-parameter limb-darkening model with the critical foreshortening angle approach (Claret 2018). The coefficients were calculated for the *TESS* passband using the same spherical PHOENIX-COND models as in Claret (2018). The applied limb-darkening coefficients were first linearly interpolated from the calculated table and then were used identically, as it is described in Section 5. Since we used *TESS* SAP fluxes, which are not corrected by the dilution factor, we used the CROWDSAP²² crowding metric value to determine the l_3 parameter for the *TESS* aperture. In the case of KELT-17b this gives $l_{3, \text{TESS}} = 0.0009$, for KELT-19Ab $l_{3, \text{TESS}} = 0.0150$, and in the case of KELT-21b $l_{3, \text{TESS}} = 0.0636$. The uncertainties in the fitted parameters were derived based on the covariance matrix method. We present the best-fitting parameters of KELT-17, KELT-19A, and KELT-21 systems in Table 8. The corresponding phase-folded transit light curves, overplotted with the best-fitting RMF models are depicted in Figs 10 and 11.

Based on the mid-transit time values T_c , presented in the Tables 5 and 8, we can clearly see that the time-baseline was extended significantly using the *TESS* data base. In the case of KELT-17b, the *TESS* data set follows the *CHEOPS* data set. The closest mid-transit time to the mid-point of *TESS* observations is $T_{c, \text{TESS}} = 2459536.27682 \pm 0.00013 \text{ BJD}_{\text{TDB}}$, while for the *CHEOPS* data set it is $T_{c, \text{CHEOPS}} = 2459215.937950 \pm 0.000086 \text{ BJD}_{\text{TDB}}$. The time-baseline of these two data sets is about 1 yr, but if we add the literature data (Zhou et al. 2016) to the data set, based on the mid-transit time of $T_{c, \text{Z2016}} = 2457226.14219 \pm 0.00033 \text{ BJD}_{\text{TDB}}$ we can extend the time-baseline by about 1989 d. In the case of KELT-19Ab, the *TESS* data set precedes *CHEOPS* observations. The mid-transit time of *TESS* data is $T_{c, \text{TESS}} = 2458503.35923 \pm 0.00017 \text{ BJD}_{\text{TDB}}$, while for the *CHEOPS* data set it is $T_{c, \text{CHEOPS}} = 2459218.17799 \pm 0.00013 \text{ BJD}_{\text{TDB}}$. The time-baseline of these two data sets is about 2 yr. Using the literature data presented by Siverd et al. (2018), we could extend this time-baseline by about 1222 d – this is the difference between the mid-transit time $T_{c, \text{S2018}} = 2457281.24953 \pm 0.00036 \text{ BJD}_{\text{TDB}}$, presented by these authors and the mid-transit time derived based on the

²¹See <https://mast.stsci.edu/portal/Mashup/Clients/Mast/Portal.html>.

²²CROWDSAP is a keyword on the header of the FITS files containing the light curves. It represents the ratio of the target flux to the total flux in the *TESS* aperture.

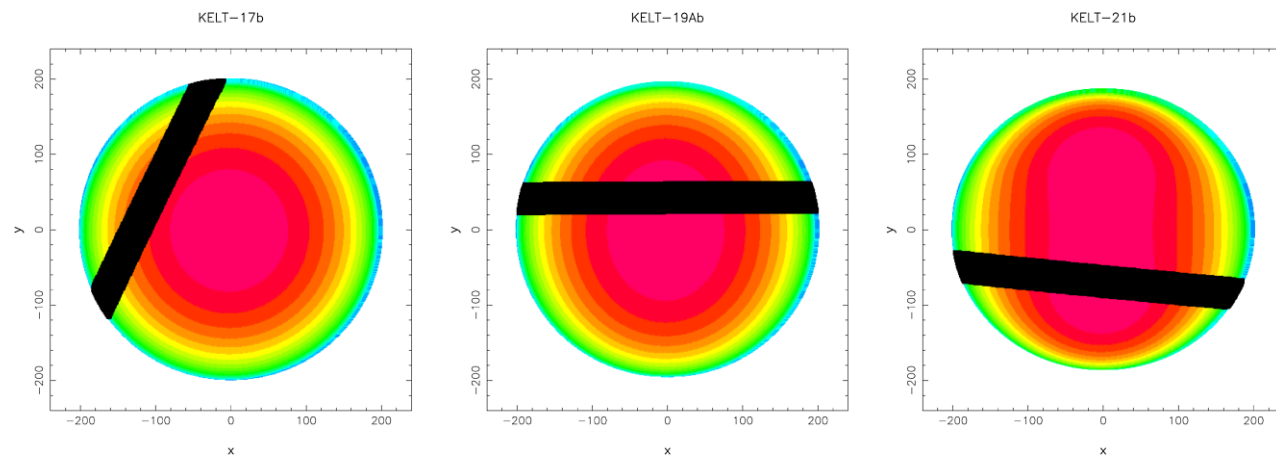


Figure 9. 2D illustration of the transit chord of KELT-17b, KELT-19Ab, and KELT-21b in front of the stellar surfaces. The intensity distribution was calculated for the effective wavelength of the *CHEOPS* instrument. The green-yellow-red-magenta colouring scheme of the stellar surfaces reflects the increasing local flux as seen by the observer. The stellar inclination is always $i_* = 90$ deg.

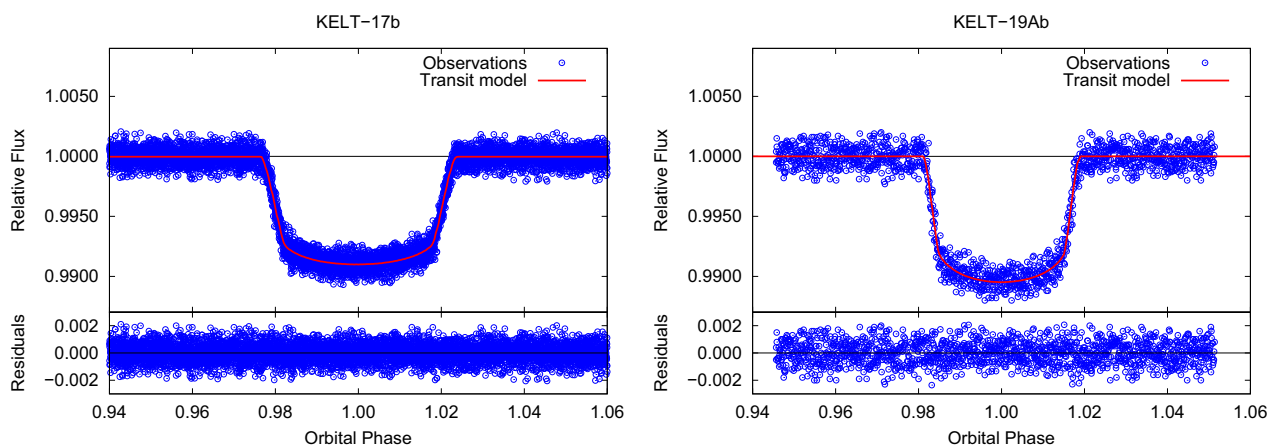


Figure 10. Phase-folded *TESS* transit light curves of KELT-17b (left-hand panel) and KELT-19Ab (right-hand panel), overplotted with the best-fitting RMF models. Residuals are also shown (bottom panels). During this modelling procedure all *TESS* data per object were fitted and the time-baseline of observations was extended for the purpose of search for TDVs.

Table 8. An overview of the RMF best-fitting parameters of the exoplanets KELT-17b, KELT-19Ab, and KELT-21b obtained from the *TESS* photometry and using the gravity-darkening approach of Espinosa Lara & Rieutord (2011). Only the fitted parameters and the l_3 parameter values are presented here. Other parameters were fixed as we presented in Table 6. Notes: ¹The closest mid-transit time to the mid-point of the *TESS* data set.

| Parameter [unit] | KELT-17b | KELT-19Ab | KELT-21b |
|--|-----------------------------|-----------------------------|-----------------------------|
| T_c [BJD _{TDB}] ¹ | $2459536.27682 \pm 0.00013$ | $2458503.35923 \pm 0.00017$ | $2459434.69341 \pm 0.00019$ |
| i [deg] | 84.537 ± 0.061 | 87.65 ± 0.36 | 86.95 ± 0.18 |
| R_s/a | 0.16141 ± 0.00063 | 0.1148 ± 0.0023 | 0.1452 ± 0.0013 |
| R_p/R_s | 0.09166 ± 0.00011 | 0.09550 ± 0.00030 | 0.09960 ± 0.00040 |
| l_{norm} | 1.0000740 ± 0.0000010 | 1.0000750 ± 0.0000010 | 1.0000740 ± 0.0000010 |
| l_3 (fixed) | 0.0009 | 0.0150 | 0.0636 |

TESS data. In the case of KELT-21b, the *TESS* data set follows the *CHEOPS* data set. Similarly, we can write the mid-transit time values of $T_{c, \text{CHEOPS}} = 2459055.352380 \pm 0.000086$ BJD_{TDB} and $T_{c, \text{TESS}} = 2459434.69341 \pm 0.00019$ BJD_{TDB}, which gives about 1 yr difference, but if we also include the data presented in the literature (Johnson et al. 2018), we can extend this time-baseline by about 1672 d ($T_{c, \text{J2018}} = 2457382.640727 \pm 0.00041$ BJD_{TDB}).

The *pyCHEOPS* software uses the transit width W as a free parameter, which corresponds to the transit duration of *CHEOPS* visits in phase

units. In the cited literature we can also find the tabulated transit duration of the exoplanets in days, which we can easily convert to the phase units. The most problematic are the *TESS* data fitted with the RMF code. This software does not use such a free parameter, therefore we directly measured the transit durations in the plots presented in Figs 10 and 11, which are also expressed in phase units. The uncertainties in these cases follow from the uncertainties of R_s/a and i (see Table 8), since these parameters affect the transit duration most significantly. In this way, we could compare the transit durations of

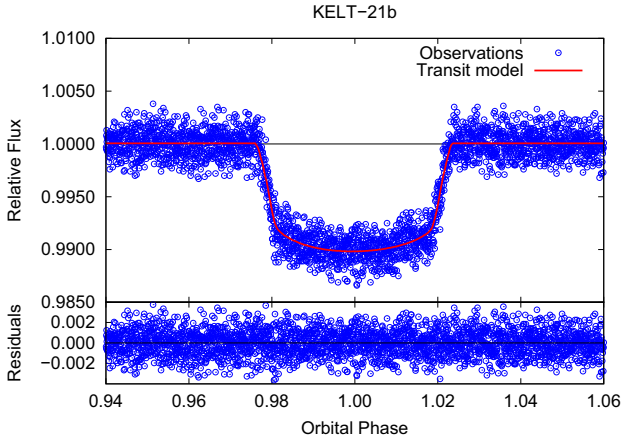


Figure 11. As in Fig. 10, but for KELT-21b.

the exoplanets coming from three seasons of observation, which is enough to uncover possible long-term TDVs – signs of orbital precession. Simultaneously, we also checked the orbit inclination angle values, because the possible orbital precession should be visible in this parameter, as well (Szabó et al. 2012, 2020). We note that the orbit inclination angle change rate di/dt parameter used by Szabó et al. (2020) is applicable only if long-term consecutive observations exist, e.g. *Kepler* observations, but this is not the case, therefore we did not apply this parameter during the analysis. The impact parameters b obtained using the *PYCHEOPS* software were converted to the orbit inclination angle values i . In such a combination of parameters, i.e. W and i , we can assume that if a long-term TDV is caused by orbital precession, a change in the parameter W is correlated with the change in parameter i . This means, for example, that if W is increasing, i is also increasing and vice versa. In the case of W and b the trend should be anticorrelated, see Szabó et al. (2012). This should be taken into consideration during the interpretation of the obtained results, which are plotted in Figs 12 and 13.

Here, we can see the transit durations W and the orbit inclination angles i in three different seasons. Since *CHEOPS* data were analysed with the *RMF* code, as well as with the *PYCHEOPS* software, we present here only the latter solution as finally adopted results. In the case of KELT-17b (Fig. 12 left-hand panel) we can see that the *CHEOPS* data reveal slightly smaller values of W and i in comparison with the discoverers, but due to the large uncertainties in the discovery

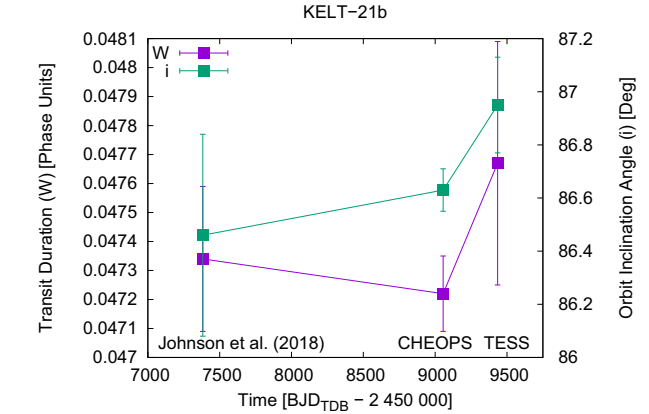
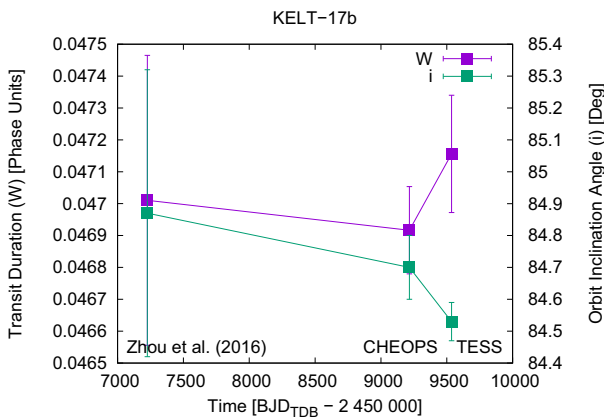


Figure 13. As in Fig. 12, but for KELT-21b.

values this difference is inconclusive. Using *TESS* observations we obtained the W and i parameter values within a 3σ agreement with the *CHEOPS* results, which means that the difference is not significant. Moreover, the parameter trends seem to be anticorrelated between the *CHEOPS* and *TESS* observations, which is against the precession-based long-term TDV, as we discussed this in the previous paragraph. KELT-19Ab is also an interesting object, since using both (*TESS* and *CHEOPS*) data sets we found the transit duration shorter and the orbit inclination angle value larger in comparison with the discovery values, see Fig. 12 right-hand panel. The difference between certain parameter values is significant, exceeding the 3σ difference, which indicates the robustness of the detection. If we took a look again at Fig. 12 right-hand panel, we can see that the trend in W and i is anticorrelated, thus the detection of the shorter transit duration compared to the discovery paper cannot be due to orbital precession. Rather, the smaller W is a consequence of a smaller planet size, as we concluded in Section 4.3.2. In the case of KELT-21b (see Fig. 13), using *CHEOPS* and *TESS* observations we found the orbit inclination angle larger in comparison with the discovery value and the transit duration is also longer based on the *TESS* measurements. Although the differences are not significant due to the larger uncertainties in the detection, we can see that the trend in W and i seems to be correlated, thus this object could be interesting from the viewpoint of long-term TDV and orbital precession in the future. More observations are needed in this case.

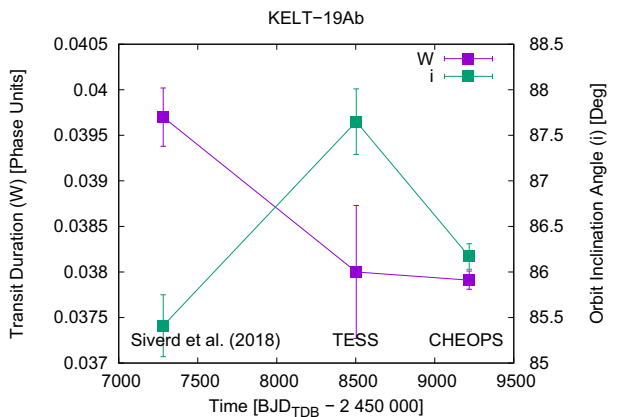


Figure 12. Transit durations and orbit inclination angles of KELT-17b (left-hand panel) and KELT-19Ab (right-hand panel) in different seasons, obtained based on literature data, *CHEOPS*, and *TESS* observations. For more details see the text of Section 6.1.

6.2 Search for TTVs – signs of additional substellar objects in the systems

To uncover the possible TTVs, which can indicate additional substellar objects, i.e. planets or brown dwarfs in the systems, we constructed the observed-minus-calculated (O-C) diagram for mid-transit times. Similarly as in Section 6.1, we used not only the *CHEOPS* observations, because of the following reasons. The interruptions occurring in *CHEOPS* visits represent a disadvantage from this viewpoint, although the data are precise. If the ingress and/or the egress part of the transit is missing, this can significantly decrease the precision of the O-C value. Another reason for use of additional observations is that more O-C data can easier uncover any periodicity coming from perturbations of an additional object in the system. Therefore, besides the *CHEOPS* data collected within this project, we also used the available *TESS* data and literature data. *CHEOPS* data were treated using the `pycheops` software as it is described in the second part of Section 4.2. During this procedure we obtained four fitted $\Delta T_{0,n}$ values, i.e. one for each visit. Since $\Delta T_{0,n}$ values correspond to the wanted O-C values of mid-transit times, we could easily get the O-C diagram of *CHEOPS* observations. Such a diagram is generated automatically by the `pycheops` software and it enabled us to first-look check these O-C data. On the other hand, we needed the ‘O’ times of individual transits with uncertainties, i.e. the $T_{0,n}$ values, since this is the input for the `OCFIT` code, described and applied later in this section. Therefore, we used equation (1) to get the observed mid-transit times of individual *CHEOPS* transits. In the next step we used the *TESS* data, already processed in Section 6.1. To obtain the ‘O’ times of the mid-transits we modelled each *TESS* transit event individually using the `RMF` code. We fixed every parameter to its best value from the joint `pycheops` model (see Table 5) except for two parameters: the mid-transit time and the light-curve normalization factor of the given transit. We summarize the *CHEOPS* and *TESS* observed mid-transit times in Table 9. Finally, to extend the time-baseline of *CHEOPS* and *TESS* observations and to increase the amount of data points, we also used the already published ‘O’ times, presented by Zhou et al. (2016), Siverd et al. (2018) and Johnson et al. (2018).

To calculate the ‘C’ times of the individual transit events and to construct the O-C diagram of mid-transit times we applied the `OCFIT`²³ code (Gajdoš & Parimucha 2019). To plot the O-C diagram of the mid-transit times it requires ‘O’ times with uncertainties, the mid-transit time T_c and the orbital period P_{orb} of the planet. Then it uses the linear ephemeris formula as:

$$T_{c,n} = T_c + P_{\text{orb}} \times E \quad (2)$$

to construct the O-C diagram, where $T_{c,n}$ corresponds to the ‘C’ value of the n -th transit, and E is the epoch of observation, i.e. the number of the orbital cycle. For P_{orb} we used the best-fitting joint `pycheops` model parameters (see Table 5), but for T_c we chose the literature values presented by Zhou et al. (2016), Siverd et al. (2018) and Johnson et al. (2018), because the derived *CHEOPS*-based T_c parameter values were located at the end/middle of the joint (literature and this work) data sets. It is better to choose the T_c parameter from the beginning of the whole data set. The obtained O-C diagrams of the planets are depicted in Figs 14 and 15. We can see that the O-C data of mid-transit times do not show periodic features, which means that there is no evidence for a third body in the planetary systems. To final check the possibility of additional

Table 9. The list of the observed (O) mid-transit times of KELT-17b, KELT-19Ab, and KELT-21b, derived in this work using the joint `pycheops` model parameter values (see Table 5). The epoch E is calculated according to the T_c parameter values, presented by Zhou et al. (2016), Siverd et al. (2018), and Johnson et al. (2018).

| E | ‘O’ times [BJD _{TDB}] | $\pm 1\sigma$ [d] | Source |
|-----------|---------------------------------|-------------------|---------------|
| KELT-17b | | | |
| 639 | 2459194.37646 | 0.00041 | <i>CHEOPS</i> |
| 641 | 2459200.53715 | 0.00016 | <i>CHEOPS</i> |
| 642 | 2459203.61727 | 0.00015 | <i>CHEOPS</i> |
| 661 | 2459262.14059 | 0.00016 | <i>CHEOPS</i> |
| 739 | 2459502.39443 | 0.00032 | <i>TESS</i> |
| 740 | 2459505.47552 | 0.00028 | <i>TESS</i> |
| 741 | 2459508.55519 | 0.00030 | <i>TESS</i> |
| 742 | 2459511.63552 | 0.00032 | <i>TESS</i> |
| 743 | 2459514.71578 | 0.00031 | <i>TESS</i> |
| 744 | 2459517.79631 | 0.00034 | <i>TESS</i> |
| 745 | 2459520.87523 | 0.00030 | <i>TESS</i> |
| 746 | 2459523.95613 | 0.00030 | <i>TESS</i> |
| 747 | 2459527.03613 | 0.00029 | <i>TESS</i> |
| 748 | 2459530.11631 | 0.00027 | <i>TESS</i> |
| 749 | 2459533.19632 | 0.00030 | <i>TESS</i> |
| 750 | 2459536.27697 | 0.00030 | <i>TESS</i> |
| 752 | 2459542.43692 | 0.00029 | <i>TESS</i> |
| 753 | 2459545.51797 | 0.00029 | <i>TESS</i> |
| 754 | 2459548.59758 | 0.00030 | <i>TESS</i> |
| 756 | 2459554.75829 | 0.00031 | <i>TESS</i> |
| 757 | 2459557.83755 | 0.00032 | <i>TESS</i> |
| 758 | 2459560.91815 | 0.00027 | <i>TESS</i> |
| 759 | 2459563.99834 | 0.00032 | <i>TESS</i> |
| 761 | 2459570.15903 | 0.00028 | <i>TESS</i> |
| 762 | 2459573.23897 | 0.00028 | <i>TESS</i> |
| 763 | 2459576.31897 | 0.00030 | <i>TESS</i> |
| KELT-19Ab | | | |
| 263 | 2458494.13568 | 0.00047 | <i>TESS</i> |
| 264 | 2458498.74760 | 0.00038 | <i>TESS</i> |
| 266 | 2458507.97115 | 0.00048 | <i>TESS</i> |
| 267 | 2458512.58297 | 0.00043 | <i>TESS</i> |
| 412 | 2459181.28423 | 0.00019 | <i>CHEOPS</i> |
| 419 | 2459213.56631 | 0.00023 | <i>CHEOPS</i> |
| 425 | 2459241.23668 | 0.00028 | <i>CHEOPS</i> |
| 426 | 2459245.84811 | 0.00031 | <i>CHEOPS</i> |
| KELT-21b | | | |
| 457 | 2459033.67650 | 0.00032 | <i>CHEOPS</i> |
| 462 | 2459051.74102 | 0.00071 | <i>CHEOPS</i> |
| 463 | 2459055.35200 | 0.00021 | <i>CHEOPS</i> |
| 472 | 2459087.86668 | 0.00046 | <i>CHEOPS</i> |
| 564 | 2459420.24231 | 0.00058 | <i>TESS</i> |
| 565 | 2459423.85549 | 0.00054 | <i>TESS</i> |
| 566 | 2459427.46758 | 0.00060 | <i>TESS</i> |
| 567 | 2459431.08095 | 0.00059 | <i>TESS</i> |
| 568 | 2459434.69341 | 0.00053 | <i>TESS</i> |
| 569 | 2459438.30580 | 0.00052 | <i>TESS</i> |
| 570 | 2459441.91831 | 0.00050 | <i>TESS</i> |
| 571 | 2459445.53197 | 0.00050 | <i>TESS</i> |

objects in the systems we fitted the O-C data sets of mid-transit times. As first we applied a linear function using the `OCFIT` package `FitLinear`. The free parameters of the linear model are the mid-transit time T_c and the orbital period P_{orb} . Subsequently, the O-C data were fitted with a quadratic function within the `OCFIT` package `FitQuad`. The free parameters of the quadratic model are the mid-transit time T_c , the orbital period P_{orb} , and the quadratic coefficient Q , see Garai et al. (2021) for more information about

²³See <https://github.com/pavolgaj/OCFit>.

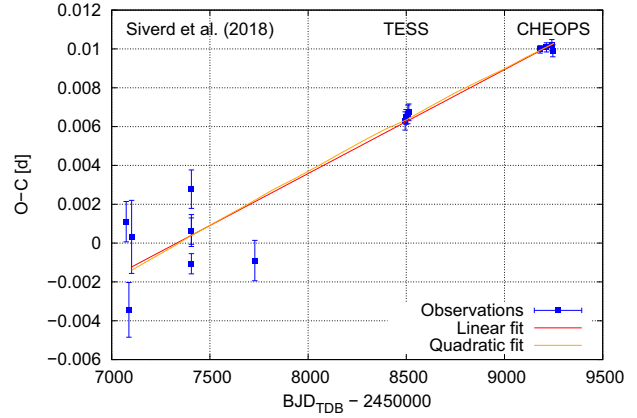
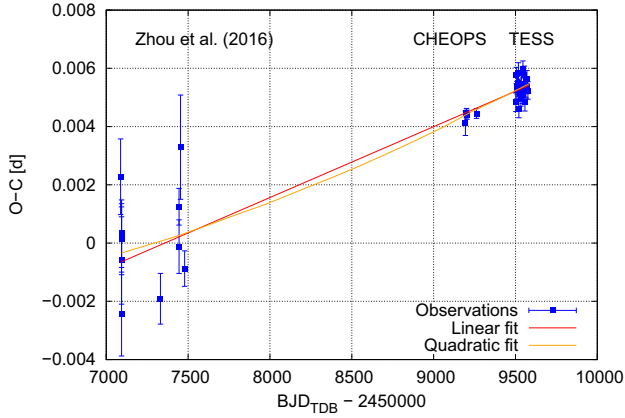


Figure 14. Observed-minus-calculated (O-C) diagrams of KELT-17b (left-hand panel) and KELT-19Ab (right-hand panel) mid-transit times, obtained based on literature data, *CHEOPS*, and *TESS* observations. For more details see the text of Section 6.2.

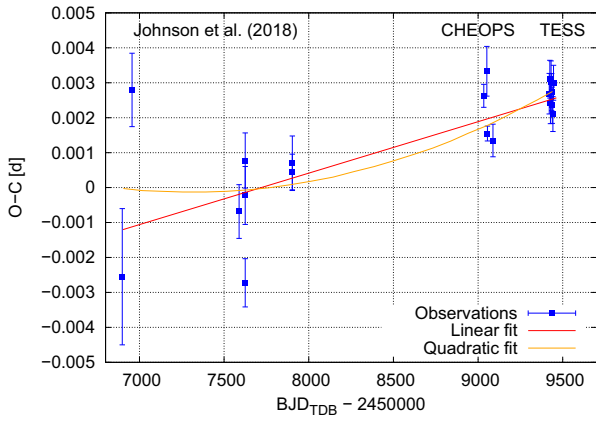


Figure 15. As in Fig. 14, but for KELT-21b.

this parameter. The uncertainties in the fitted parameters of P_{orb} , T_c , and Q were derived within the OCFIT packages `FitLinear` and `FitQuad`, applying the covariance matrix method. These fits are also visible in Figs 14 and 15. The quality of the linear and quadratic fits was expressed as Bayesian Information Criterion (BIC), which is defined as:

$$BIC = \chi^2 + k \ln N, \quad (3)$$

where k is the number of free parameters of the model and N is the number of data points.

In the case of KELT-17b the observations cover a time-baseline of about 2400 d, but the literature data have significant scatter compared to the *CHEOPS* and *TESS* data. There is no significant difference between the Bayesian Information Criterion when we apply linear, or quadratic fit ($BIC_{\text{lin}} = 59.0$ and $BIC_{\text{quad}} = 60.3$, respectively), therefore the quadratic fit is not justified here. The O-C values obtained by the discoverers allowed to exclude periodic TTVs with the semi-amplitude of about 5 min. If we take into consideration *CHEOPS* and *TESS* observations, we can put more constraints on this upper limit with the value of about 3 min (3σ upper limit). Based on the linear fit we obtained a new linear ephemeris of KELT-17b, which is presented in Table 10. For KELT-19Ab we collected transit observations covering a time baseline of about 2000 d, including the literature data. The O-C data have a well defined and clearly visible linear trend, see Fig. 14 (right-hand panel). There is no significant difference between the linear and

Table 10. Linear ephemeris of KELT-17b, KELT-19Ab, and KELT-21b, obtained based on the whole O-C data-set of mid-transit times. Here, we improved further the orbital period of the planets compared to the joint `PYCHEOPS` solutions (see and compare the appropriate parameter values with Table 5), thus the final P_{orb} values are presented in this table.

| Parameter [unit] | Value | $\pm 1\sigma$ |
|-----------------------------|---------------|---------------|
| KELT-17b | | |
| T_c [BJD _{TDB}] | 2457226.14186 | 0.00041 |
| P_{orb} [d] | 3.08017988 | 0.00000058 |
| KELT-19Ab | | |
| T_c [BJD _{TDB}] | 2457281.24924 | 0.00069 |
| P_{orb} [d] | 4.6117352 | 0.0000018 |
| KELT-21b | | |
| T_c [BJD _{TDB}] | 2457382.64023 | 0.00083 |
| P_{orb} [d] | 3.6127693 | 0.0000017 |

quadratic fit, the Bayesian Information Criterion are very similar, i.e. $BIC_{\text{lin}} = 39.7$ and $BIC_{\text{quad}} = 42.0$, therefore we adopted the linear fit as a final solution. The obtained linear ephemeris is presented in Table 10. Taking the precise *CHEOPS* and *TESS* observations into consideration, we can exclude periodic TTVs with a semi-amplitude of about 3 min (3σ upper limit), which is an improvement by a factor of 2 in comparison with the discovery O-C values. In the case of KELT-21b there are observations from three seasons, as well, which cover a time-baseline of about 2000 d. The relative scatter of the *CHEOPS* and *TESS* data is larger in comparison with the previous case. On the other hand, the newly obtained O-C data are more precise than the discovery data, see Fig. 15. The quadratic trend is not significant, i.e. there is no significant difference between the Bayesian Information Criterion of the linear and the quadratic fit ($BIC_{\text{lin}} = 54.6$ and $BIC_{\text{quad}} = 53.6$, respectively). Since no statistical justification for the quadratic fit, we can adopt the linear fit as a final solution. The obtained linear ephemeris is presented in Table 10. Based on the *CHEOPS* and *TESS* O-C data we did not find periodic TTVs with a semi-amplitude larger than 3 min (1σ upper limit). Since the relatively larger scatter in the new data sets, more and precise observations are needed to improve this value. In summary, we did not find any convincing evidence for an additional object in these systems, but via this procedure we improved further the orbital period of the planets (see Table 10 and compare the P_{orb} values to those of presented in Table 5). Therefore, we can

consider the P_{orb} parameter values presented in Table 10 as the final solutions.

7 CONCLUSIONS

Using precise *CHEOPS* and *TESS* photometric observations, complemented with target spectroscopy, we analysed three rapidly rotating planetary systems, i.e. KELT-17, KELT-19A, and KELT-21 from several viewpoints. We obtained new spectroscopic observations, which we used to derive stellar parameters of the planet hosts. Since the high effective temperature and the rapid rotation of the stars, the spectroscopic modelling was challenging in these cases and the resulting stellar parameters are not so precise as we expected before. On the other hand, based on the *CHEOPS* photometric observations we were able to derive significantly improved system parameters in comparison with the previously published values. Based on these results we can conclude that KELT-17b and KELT-19Ab have smaller planet radius as found before, but in the case of KELT-17b this could be also due to the parameter degeneracy. For KELT-21b we could confirm the previously obtained system and planet parameters within 3σ . The *CHEOPS* light curves were also analysed from the viewpoint of spin-orbit misalignment. Here, we were able to confirm only that the gravity-darkening effect is very low in these cases. *CHEOPS* data are too noisy to draw any conclusions on spin-orbit misalignment from the photometry alone. In addition, based on these analyses we can report on a tentative indication that the stellar inclination of KELT-21 is $I_* \approx 60$ deg.

The *CHEOPS* photometric observations, complemented with the available *TESS* data were also used to search for TDVs and TTVs in the systems. The search for long-term TDVs in the systems was motivated by the Kepler-13A planetary system, where orbital precession was identified, causing a long-term trend in the transit duration. In the cases of KELT-17b and KELT-19Ab we were able to exclude long-term TDVs causing orbital precession. The shorter transit duration of KELT-19Ab compared to the discovery paper is probably a consequence of a smaller planet radius. In the case of KELT-21b, there is an indication that a long-term TDV may exist in a connection with orbital precession, therefore this system could be interesting from this viewpoint. More high-quality data are needed in the future to confirm, or reject the orbital precession/long-term TDV. Furthermore, via observed-minus-calculated diagrams of mid-transit times we probed the photometry data from the viewpoint of additional objects in the systems, but we did not find any convincing evidence. Based on the *CHEOPS* and *TESS* observations we set new upper limits on possible TTV semi-amplitudes and we were able to improve further the orbital period of the planets.

ACKNOWLEDGEMENTS

We thank the anonymous reviewer for the helpful comments and suggestions. We also thank Dr. K. G. Isaak, the ESA *CHEOPS* Project Scientist, responsible for the ESA *CHEOPS* Guest Observers Programme, for the helpful discussions and support. This work was supported by the Hungarian National Research, Development and Innovation Office (NKFIH) grant K-125015, the PRODEX Experiment Agreement No. 4000137122 between the ELTE University and the European Space Agency (ESA-D/SCI-LE-2021-0025), the City of Szombathely under agreement No. 67.177-21/2016, and by the VEGA grant of the Slovak Academy of Sciences No. 2/0031/22. TP acknowledges support from the Slovak Research and Development Agency – contract No. APVV-20-0148. AC acknowledges financial support from the State Agency for Research of the Spanish MCIU

through the ‘Center of Excellence Severo Ochoa’ award for the Instituto de Astrophysics of Andalusia (SEV-2017-0709). *CHEOPS* is an ESA mission in partnership with Switzerland with important contributions to the payload and the ground segment from Austria, Belgium, France, Germany, Hungary, Italy, Portugal, Spain, Sweden, and the UK. The authors acknowledge the observing time awarded within the *CHEOPS* Guest Observers Programme No. 1 (AO-1) and the support from the Science Operations Centre. This paper includes data collected with the *TESS* mission, obtained from the MAST data archive at the Space Telescope Science Institute (STScI). Funding for the *TESS* mission is provided by the NASA Explorer Program. STScI is operated by the Association of Universities for Research in Astronomy, Inc., under NASA contract NAS 5-26555. This work has used data from the European Space Agency (ESA) mission *Gaia* (<https://www.cosmos.esa.int/gaia>), processed by the *Gaia* Data Processing and Analysis Consortium (DPAC, <https://www.cosmos.esa.int/web/gaia/dpac/consortium>). Funding for the DPAC has been provided by national institutions, in particular the institutions participating in the *Gaia* Multilateral Agreement.

DATA AVAILABILITY

The data underlying this article will be shared on reasonable request to the corresponding author. The reduced light curves presented in this work will be made available at the CDS (<http://cdsarc.u-strasbg.fr/>).

REFERENCES

- Ahlers J. P. et al., 2020, *AJ*, 160, 4
 Anderson D. R. et al., 2018, preprint ([arXiv:1809.04897](https://arxiv.org/abs/1809.04897))
 Andreasen D. T. et al., 2017, *A&A*, 600, A69
 Barnes J. W., 2009, *ApJ*, 705, 683
 Barnes J. W., Linscott E., Shporer A., 2011, *ApJS*, 197, 10
 Barros S. C. C., Demangeon O., Díaz R. F., Cabrera J., Santos N. C., Faria J. P., Pereira F., 2020, *A&A*, 634, A75
 Baudrand J., Bohm T., 1992, *A&A*, 259, 711
 Benz W. et al., 2021, *Exp. Astron.*, 51, 109
 Blanco-Cuaresma S., 2019, *MNRAS*, 486, 2075
 Blanco-Cuaresma S., Soubiran C., Heiter U., Jofré P., 2014, *A&A*, 569, A111
 Bonfanti A. et al., 2021, *A&A*, 646, A157
 Borsato L. et al., 2021, *MNRAS*, 506, 3810
 Borucki W. J., Dunham E. W., Koch D. G., Cochran W. D., Rose J. D., Cullers D. K., Granados A., Jenkins J. M., 1996, *Ap&SS*, 241, 111
 Borucki W. et al., 2004, in Favata F., Aigrain S., Wilson A., eds, *ESA SP-538: Stellar Structure and Habitable Planet Finding*. ESA, Noordwijk, p. 177
 Claret A., 1998, *A&AS*, 131, 395
 Claret A., 2012, *A&A*, 538, A3
 Claret A., 2018, *A&A*, 618, A20
 Dawson R. I., Johnson J. A., Morton T. D., Crepp J. R., Fabrycky D. C., Murray-Clay R. A., Howard A. W., 2012, *ApJ*, 761, 163
 Donati J. F., Semel M., Carter B. D., Rees D. E., Collier Cameron A., 1997, *MNRAS*, 291, 658
 Espinosa Lara F., Rieutord M., 2011, *A&A*, 533, A43
 Foreman-Mackey D., Hogg D. W., Lang D., Goodman J., 2013, *PASP*, 125, 306
 Foreman-Mackey D., Agol E., Ambikasaran S., Angus R., 2017, *AJ*, 154, 220
Gaia Collaboration, 2018, *A&A*, 616, A1
 Gajdoš P., Parimucha Š., 2019, *Open Eur. J. Var. Stars*, 197, 71
 Gajdoš P. et al., 2019, *MNRAS*, 484, 4352
 Garai Z. et al., 2017, *Astron. Nachr.*, 338, 75
 Garai Z. et al., 2021, *MNRAS*, 508, 5514
 Gaudi B. S. et al., 2017, *Nature*, 546, 514
 Gillon M. et al., 2012, *A&A*, 542, A4

- Gillon M. et al., 2014, *A&A*, 562, L3
 Gonzalez G., Laws C., 2000, *AJ*, 119, 390
 Gonzalez G., Vanture A. D., 1998, *A&A*, 339, L29
 Gray R. O., Corbally C. J., 1994, *AJ*, 107, 742
 Hartman J. D. et al., 2014, *AJ*, 147, 128
 Hebb L. et al., 2009, *ApJ*, 693, 1920
 Hébrard G. et al., 2009, in Pont F., Sasselov D., Holman M. J., eds, Proc. IAU Symp. 253, *Transiting Planets*. Cambridge Univ. Press, Cambridge, p. 508
 Hellier C. et al., 2009, *Nature*, 460, 1098
 Hoyer S., Guterman P., Demangeon O., Sousa S. G., Deleuil M., Meunier J. C., Benz W., 2020, *A&A*, 635, A24
 Høg E. et al., 2000, *A&A*, 355, L27
 Johnson J. A. et al., 2011, *ApJ*, 735, 24
 Johnson M. C., Cochran W. D., Albrecht S., Dodson-Robinson S. E., Winn J. N., Gullikson K., 2014, *ApJ*, 790, 30
 Johnson M. C. et al., 2018, *AJ*, 155, 100
 Kallinger T. et al., 2014, *A&A*, 570, A41
 Knutson H. A. et al., 2014, *ApJ*, 785, 126
 Kraft R. P., 1967, *ApJ*, 150, 551
 Lendl M. et al., 2020, *A&A*, 643, A94
 Luger R., Foreman-Mackey D., Hogg D. W., 2017, *Res. Notes Am. Astron. Soc.*, 1, 7
 Maciejewski G. et al., 2013, *A&A*, 551, A108
 Masuda K., 2015, *ApJ*, 805, 28
 Maxted P. F. L., 2018, *A&A*, 616, A39
 Maxted P. F. L., Gill S., 2019, *A&A*, 622, A33
 Maxted P. F. L. et al., 2022, *MNRAS*, in press
 McLaughlin D. B., 1924, *ApJ*, 60, 22
 Mészáros S. et al., 2012, *AJ*, 144, 120
 Munari U., Sordo R., Castelli F., Zwitter T., 2005, *A&A*, 442, 1127
 Narita N., Sato B., Ohshima O., Winn J. N., 2008, *PASJ*, 60, L1
 Nascimbeni V. et al., 2013, *A&A*, 549, A30
 Neveu-VanMalle M. et al., 2016, *A&A*, 586, A93
 Oberst T. E. et al., 2017, *AJ*, 153, 97
 Pál A., Kocsis B., 2008, *MNRAS*, 389, 191
 Pribulla T., 2012, in Richards M. T., Hubeny I., eds, IAU Symp. Vol. 282, *From Interacting Binaries to Exoplanets: Essential Modeling Tools*. Cambridge Univ. Press, Cambridge, p. 279
 Pribulla T. et al., 2015, *Astron. Nachr.*, 336, 682
 Pych W., 2004, *PASP*, 116, 148
 Ricker G. R., 2014, *J. Am. Assoc. Var. Star Obs.*, 42, 234
 Ridden-Harper A., Turner J. D., Jayawardhana R., 2020, *AJ*, 160, 249
 Rossiter R. A., 1924, *ApJ*, 60, 15
 Rucinski S. M., 1992, *AJ*, 104, 1968
 Santos N. C. et al., 2013, *A&A*, 556, A150
 Seeliger M. et al., 2014, *MNRAS*, 441, 304
 Siverd R. J. et al., 2018, *AJ*, 155, 35
 Szabó G. M. et al., 2011, *ApJ*, 736, L4
 Szabó G. M., Pál A., Drekas A., Simon A. E., Szalai T., Kiss L. L., 2012, *MNRAS*, 421, L122
 Szabó G. M., Pribulla T., Pál A., Bódi A., Kiss L. L., Drekas A., 2020, *MNRAS*, 492, L17
 Tsantaki M., Andreasen D. T., Teixeira G. D. C., Sousa S. G., Santos N. C., Delgado-Mena E., Bruzual G., 2018, *MNRAS*, 473, 5066
 Turner J. D., Ridden-Harper A., Jayawardhana R., 2021, *AJ*, 161, 72
 Valenti J. A., Piskunov N., 1996, *A&AS*, 118, 595
 Von Zeipel H., 1924a, *MNRAS*, 84, 665
 Von Zeipel H., 1924b, *MNRAS*, 84, 684
 Wang X.-Y. et al., 2018, *PASP*, 130, 064401
 Yang F., Chary R.-R., Liu J.-F., 2022, *AJ*, 163, 42
 Zahn J. P., Ranc C., Morel P., 2010, *A&A*, 517, A7
 Zhou G. et al., 2016, *AJ*, 152, 136

This paper has been typeset from a $\text{\TeX}/\text{\LaTeX}$ file prepared by the author.